Computational Study of the Flowfield Through a Cascade of NACA 0012 Airfoils

by

Muhammad Naweed Ahmed

A Thesis Presented to the

FACULTY OF THE COLLEGE OF GRADUATE STUDIES

KING FAHD UNIVERSITY OF PETROLEUM & MINERALS

DHAHRAN, SAUDI ARABIA

In Partial Fulfillment of the
Requirements for the Degree of

MASTER OF SCIENCE

In

MECHANICAL ENGINEERING

December, 1995

Computational Study of the Flowfield Through a Cascade of NACA 0012 Airfoils

BY

Muhammad Naweed Ahmed

A Thesis Presented to the

FACULTY OF THE COLLEGE OF GRADUATE STUDIES

KING FAHD UNIVERSITY OF PETROLEUM & MINERALS

DHAHRAN, SAUDI ARABIA

In Partial Fulfillment of the
Requirements for the Degree of

MASTER OF SCIENCE
In
Mechanical Engineering

December 1995

KING FAHD UNIVERSITY OF PETROLEUM AND MINERALS

DHAHRAN, SAUDI ARABIA

COLLEGE OF GRADUATE STUDIES

This thesis, written by

Muhammad Naweed Ahmed

under the direction of his Thesis Advisor, and approved by his Thesis committee, has been presented to and accepted by the Dean, College of Graduate Studies, in partial fulfillment of the requirements for the degree of

MASTER OF SCIENCE IN MECHANICAL ENGINEERING

Thesis Committee :

Dr. Bekir Sami Yilbas (Chairman)

Dr. Mohammad O. Budair (Co-Chairman)

Department Chairman (Mech. Engg.)

Dr. Mohamed Abdel-Aziz Habib (Member)

Dean, College of Graduate Studies

Dr. Ahmet Ziyaettin Sahin (Member)

Date: 20/3/96

Dedicated to

My Loving Parents

Acknowledgment

In the name of Allah, Most Gracious, Most Merciful. Read in the name of thy and Cherisher, Who created. Created from a {*leech-like* } clot. Read and thy Lord is Most Bountiful. He Who taught {the use of} the pen. Taught man that which he knew not. Nay, but doth transgress all bounds. In that he looketh upon as self-sufficient. Verily, to thy is the return {all}.

(The Quran, Surah 96)

First and foremost, all praise to Allah, *subhanahu-wa-ta'ala*, Almighty, Who gave me an opportunity, and patience to carry out this work. I priviledged to His name in the way through accomplishment.
I seek mercy, favor, and forgiveness. And I ask to accept my little effort.
May He, *subhanahu-wa-ta-Aaala*, guide us and the humanity to the right path *(Aameen)*.

Acknowledgement is due to King Fahd Universitof Petroleum & Minerals for providing support to this research work.

I am indebted to my thesis chairman, Dr.Bekir Sami Yilbas for help and advice. I acknowledge him for his valuable time, encouragement and guidance especially throughout my study in KFUPM as an MS student. Working with him was indeed a experience.

I grateful to my thesis comittee member, Dr. Mohammad O. Budair for his deep interest, constructive criticism and encouragement during the course of this work. Thanks are also due to the my thesis committee member, Dr.Habib and Dr Sahin for their comments and critical review of the thesis. I am thankful to the other faculty members for their cooperation.

I thankful to my fellograduate students and my friends on the campus especially Asim, Amir, Asif, Ikram, Rashid and Ayaz who provided a wonderful company.

Thanks are due to the members of my family for their and moral support throughout my academic career. No pdevelopment could ever take place without the proper of parents. This work dedicated to my parents for taking pains to my academic pursuits and my personality. I acknowledge with gratitude, the and encouragement of my members that helped me overcome homesicand concentrate on my work.

Contents

List of Tables

List of Figures

Abstract

Name: Muhammad Naweed Ahmed

Title: Computational Study of the Flowfield Through a Cascade of NACA 0012 Airfoils

Major Field: Mechanical Engineering

Date of Degree: December, 1995

Numerical simulation of flow past airfoils is important in the aerodynamic design of aircraft wings and turbomachinery components. These lifting devices often attain optimum performance at the condition of onset of separation. Therefore separation phenomena must be included if the analysis is aimed at practical applications. Consequently, in the present study, numerical simulation of steady flow in a linear cascade of NACA 0012 airfoils is accomplished using a numerical scheme employing control volume approach. The flow field is determined by solving two dimensional incompressible Navier-Stokes equations while the effects of turbulence are accounted for by the k-ϵ model. Separation point at the airfoil surface is predicted at high angles of attack. Pressure, lift and drag coefficients are computed and the results are compared with the predictions of isolated single NACA 0012 airfoil. The study is extended to include the effects of stagger angle of the cascade and rotating boundaries of the isolated airfoil on the flow characterstics. It is found that increase in solidity and/or stagger angle increases the angle of attack at which separation occurs and pressure, lift and drag coefficients are highly influenced by the angle of attack and the solidity ratios. For the case of airfoil leading edge rotation a reduction in the wake size is predicted at high angle of attack. For this case an increase in the lift and a decrease in the drag coefficient is also predicted.

Master of Science Degree
King Fahd University of Petroleum and Minerals
Dhahran, Saudi Arabia
December, 1995

خلاصة الرسالة

الإسم : محمد نوير أحمد

العنوان : دراسة رقمية لإنسياب المائع حول عمود من أجنحة ناي ١٢ ٠٠

التخصص : هندسة ميكانيكية

تاريخ الشهادة : ديسمبر ١٩٩٥م

إن دراسة إنسياب المائع حول الأجنحة معهم في مجال التصميم الإنسيابي لأجنحة الطائرات وأجزاء أخرى من الأجهزة الهوائية وهذه الأجهزة غالبا تصل إلى أفضل فعالية لها مثل بدء السائل بالإنفصال عنها ولهذا فإنه خاصة إنفصال السائل عن الجسم لابد من دراستها إذا كنا نريد دراسة خواص هذه الأجنحة بفعالية ٠

وبالتالي فإن هذه الدراسة سوف ندرس رقميا الإنسياب الثابت الزمني خلال عمود خطي من أجنحة ناكا ١٢ ٠٠ ، بإستخدام طريقة الإحداثيات المنحنية تم تحديد المجال الإنسيابي للمائع بحمل معادلات تغير ستكوكس من الدرجة الثانية وبأدخال تأثير السريان المضطرب بادخال نموذج (٤ - ١٢) ٠ تم أيضا تحديد نقطة انفصال السائل لأجنحة ذات ميل عال في مواجهة السائل ٠

تم أيضا حساب قيم الضغط معامل الدفع ومعامل التراجح وتمت بالنتائج المتوفرة من خلال انسياب المائع حول جناح ناكا ١٢ واحد ٠ وفي هذا البحث تم أيضا إضافة تأثير زاوية ستقر لعمود الأجنحة ودورات الأطراف لجناح واحد معزول على خواص جريان المائع ٠ لقد وجد من خلال هذا البحث أن زيادة الصلابة أو زاوية الميلان يزيد من زاوية المواجهة والتي يحدث عندها انفصال السائل ٠ وكذلك فإن الضغط ومعامل الدفع والإرتجاع يتأثران تأثرا كبيرا بزاوية المواجهة ومعاملات الصلابة ٠ وخلال حالة الجناح المتقدم الدوران فإن نقصان في حجم الأضطرب قد لوحظ عند زيادة زاوية المواجهة ٠ وفي نفس الحالة لوحظ زيادة في معامل الدفع وانخفاظ في معامل التراجع قد تم ملاحظته ٠

درجة الماجستير في العلوم

جامعة الملك فهد للبترول والمعادن

الظهران - المملكة العربية السعودية

ديسمبر ١٩٩٥م

Nomenclature

C	chord legth (m)
C/S	solidity ratio
C_d	coefficient of drag, $C_d = \frac{D}{\rho U_\infty^2 c/2}$
C_e	convective flux, $C_e = \rho u \phi \Delta \eta$
C_l	coefficient of lift, $C_l = \frac{L}{\rho U_\infty^2 c/2}$
C_p	coefficient of pressure, $C_p = \frac{p - p_\infty}{\rho U_\infty^2/2}$
C_μ, C_1, C_2	Constants in k-ϵ turbulence model
$C_{\epsilon_1}, C_{\epsilon_2}$	Constants in k-ϵ turbulence model
D	Drag force (N)
E	roughness parameter (law of the wall)
f_1, f_2, f_μ	Constants in k-ϵ turbulence model
G	Production of turbulent kinetic energy (Joule/sec)
J	total flux across a face of the finite control volume (Kg/sec)
k	kinetic energy of turbulence (Joule)
L	Lift force (N)
M	Mach number, $M = \frac{V}{\gamma RT}$
p	local static pressure ($\frac{N}{m^2}$)
P_e	Peclet number, $P_e = \frac{\rho u \Delta \xi}{\Gamma_o}$

Pr	Prandtl number, $Pr = \frac{\mu C_p}{k}$
Re	Reynolds number, $Re = \frac{\rho VC}{\mu}$
S_ϕ	source or sink of variable ϕ
t	time (sec)
T_w	shear stress at the wall (N/m^2), $T_w = \mu \frac{du}{dy}$
U_i, u_i	cartesian velocity components (m/sec)
u_i'	turbulent fluctuating velocity components (m/sec)
x_i	Cartesian coordinate directions
x/c	nondimensional chord length

Greek Symbols

ρ	Density (Kg/m^3)
α	angle of attack (degree)
δ	Deviation angle (degree)
Γ_ϕ	Exchange coefficient for ϕ
∇	gradient/divergence operator
ϵ	dissipation rate of turbulence energy (Joule/sec)
ϵ_s	Deflection angle at stall point (degree)
κ	von karman constant (law of the wall)
μ	dynamic viscosity (kg/sec m)
ν	kinematic viscosity (m^2/sec), $\nu = \frac{\mu}{\rho}$

ξ, η	orthogonal coordinate directions
ξ	Stagger angle (degree)
ρ	density (kg/m^3)
$\sigma_k, \sigma_\epsilon$	constants in turbulence models
ϕ	general transport variable

Subscripts

E, N, S, W	values at east, north, south and west node poins
e, n, s, w	values at east, north, south and west edges of the cells
i, j	tensor subscript notation
P	values at node point p
t	turbulent
w	wall

Superscripts

*	guessed value
′	Correction in value

Chapter 1

Introduction

1.1 Cascade Flows

A cascade is a row of geometrically similar blades arranged at equal distances from each other and aligned to the flow direction as shown in figure (1.1) taken from ref. [1]. The row of blades is installed over a turn-table at the end of a wind tunnel channel such that the angle of incidence of blades with respect to the approaching flow may be varied. Vertical traverse between successive blades may then be made with pitot tubes and yaw meters to determine pressure losses and air flow angles. The schematic shown is known as a linear cascade and can be imagined as a row of compressor blades unwound from the rotor to form the cascade. The number of blades comprising the cascade has to be sufficient to eliminate any wind tunnel wall boundary layer effects and suction slots are often let into the tunnel walls to control

the boundary layer.

1.2 Evolution of Cascade testing

Axial flow steam turbines were developed in the late nineteenth century without recourse to cascade model and often with little understanding of the fluid mechanics involved. Trial and error process resulted in adequate performance for power generation and eventually propulsion. In the early part of this century the first primitive cascade wind tunnels called nozzle testers were developed to consolidate the advances and provide data for machines of higher rating and increased efficiency.

Turbines, at least while the flow is subsonic, have reasonable tolerance to the blade design and alignment errors. The same can not be said of the axial flow compressors, fans, or pumps. These operate under adverse pressure gradient. In such a diffusing flow, the danger of flow separation is much more pronounced. Most early axial flow compressors were designed badly because the necessary aerodynamics knowledge was simply not available.

During the first two decades of this century the need for an aerodynamic approach to the design of turbines and compressors was gradually realized. The design

Figure 1.1: A Cascade

of wings and isolated airfoils was well understood and attempts had been made to apply the isolated airfoil approach to turbomachines. However, this had failed even in the design of air screws.

Wood, Bradfield and Barker [2] in 1919 realized that the interference of neighboring blades should be applied to airscrew theory and modified lift coefficient in the first known cascade tests. They found that the cascade effect accounted for by far the largest part of the unexplained discrepancy between simple airfoil theory and air screw experiment.

In 1928 extensive cascade investigations were reported by Christiani [2] in Germany and by Harris and Fairthorne [2] in England. British axial compressor designs of the late 1930's used the Harris and Fairthorne data which were adequate for the development of the first axial machines having reasonable efficiency.

The last known pre-war cascade tests were performed in Japan by Shinooyama, in 1937. The earliest correlation of compressor cascades was by Howell [2] and has been widely used in axial compressor design.

As a result of systematic improvement of the aerodynamic art and the more urgent compilation of cascade data under wartime pressures, it became possible to

design an efficient axial flow compressor. The foundations were laid for the modern gas turbine and virtually all design work on axial flow machines since has been built upon that foundation.

With the development of high speed computers, computational Fluid Dynamics is emerging as an equally important tool. Especially after 1970's there has been significant advancements in non-physical analysis of cascades. This has provided an increased understanding of the flow behavior and hence improved design. At present CFD is rapidly growing and it can be anticipated that it will eventually replace the physical model testing in many of the cases.

1.3 Cascade: Merely a model to actual situation

It is important to emphasize at the outset that the cascade is merely a model. In fluid dynamics the process of modelling is one of the physical and mathematical simplifications and is intended to result in rationalization and a deeper appreciation to the actual flow situation.

The basic information required by the design of turbomachines takes, for a given blade shape, the form of graphs showing the variation of outlet angle and total

pressure loss with inlet angle while such parameters as stagger, space-chord ratio, Reynolds number and free stream turbulence level are varied. In general there are too many variables for such design information to be obtained from systematic testing of turbine and compressor rigs. Any attempts to do so usually introduces a wide range of uncertainty resulting from other spurious effects in a three dimensional rotating blade row. For this reason successful designs were not forthcoming until suitable data became available from the testing of two dimensional cascades.

1.4 Nomenclature of Cascade

Before venturing further into the analysis, it is necessary to define various important angles relevant to the design. In figure (1.2) a cambered blade is shown with a curved camber line through the centre.

The tangents to the camber line at inlet and outlet are the camber angles α'_1 and α'_2 to the axial direction respectively. The blade camber angle θ is defined as $(\alpha'_1 - \alpha'_2)$. The chord c is the distance between blade inlet and trailing edge. The stagger angle ξ is that between the axial direction and the chord and represents the angle at which the blade is set in the cascade. The blade spacing s represents the blade pitch. If the air enters with velocity c_1 at angle α_1, the angle of incidence is

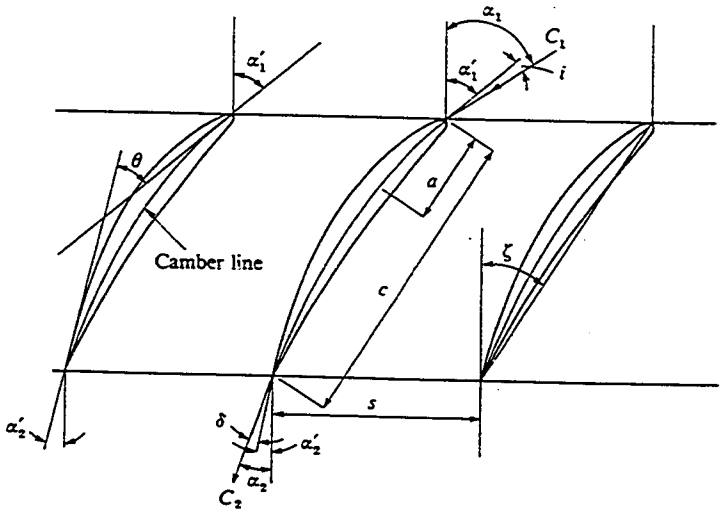

Figure 1.2: Cascade Nomenclature

$(\alpha_1 - \alpha_1')$. The air leaves the blade with velocity c_2 at angle α_2 and the difference is the deviation angle δ. The deflection increases with angle of incidence upto a maximum ϵ_s. This is the stall point where separation occurs on the suction surface of the blade.

1.5 Performance Parameters

The pressure distribution on the surface and lift and drag characteristics of cascade airfoils are of major interest to designer. To obtain generality these characteristics are represented in non-dimensional form.

The coefficient of pressure is defined as [3]

$$C_p = \frac{p - p_\infty}{\rho U_\infty^2/2} \tag{1.1}$$

Here p_∞ is the static pressure of the approaching flow upstream, and U_∞ is its velocity.

Coefficient of lift is defined as

$$C_l = \frac{L}{\rho U_\infty^2 c/2} \tag{1.2}$$

The lift L is the total force per unit length that acts on the airfoil surface in a direction perpendicular to the direction of approaching flow and c is the chord length of the airfoil.

The coefficient of drag is defined as

$$C_d = \frac{D}{\rho U_\infty^2 c/2} \tag{1.3}$$

where the drag is the total force per unit length that acts on the airfoil in the direction of the approaching flow. It is composed of two parts. One is due to the thickness and the camber of the airfoil and is called "Form Drag" whereas the other is due to frictional effects within the boundary layer surrounding the airfoil and is called "Frictional Drag".

Chapter 2

Literature Review

Rizzetta and Visbal [4] made comparative numerical study of two turbulence models for airfoil static and dynamic stall. He compared Baldwin Lomax model with the k-ϵ model of Launder and Sharma. The results indicated that k-ϵ model had better predictive capabilities.

Day [5] conducted studies on two laboratory test compressors to investigate the process leading to the formation of finite amplitude rotating stall cells. The measurements were obtained from circumferential arrays of hot wires. Flow was analyzed both spatially and temporaly to show that the modal perturbations were not always present prior to stall. The measurements led to the conclusion that the occurrence of modal perturbations and the formation of finite amplitude stall cells were two separate phenomena both occurring roughly under the same conditions at the peak

of pressure rise characteristics. Hence measurements confirmed the unsuspected importance of short length scale disturbances in the process of stall inception. It is interesting to note that this small disturbance idea was first proposed by Emmons, decades ago.

Koc et al. [6] examined the stall behavior of an isolated compressor rotor experimentally. They showed that average flow measurements during full span stall supported the view that the unstalled part of the blading must operate at flows beyond the partial stall zone region.

Davidson and Rizzie [7] predicted numerically stall over a two dimensional airfoil. They used a standard explicit Runge Kutta time marching code. They made the use of three different turbulence models. Flow conditions were set as Re=$2.1*10^6$ with M=0.25 and angle of attack varied from 9^0 to 19^0. Baldwin Lomax model and standard k-ϵ model were shown to fail predicting stall whereas Algebraic Stress Model (ASM) did predict stall at 16^0 which was found to be in good agreement with experimental observations. As the ASM is valid only for fully turbulent flows, it was matched with a one equation model close to the wall. The main reason for the superiority of ASM was believed to be its ability to take into account the influence of wall curvature and the large difference in the normal Reynolds stresses. The amount of computational time consumed was sufficiently higher than k-ϵ or Baldwin

Lomax model because of a complicated start-up procedure and large separation zone.

Hoffmann [8] made measurements on the lift and the drag characteristics and associated flow field over the suction surface of a NACA 0015 airfoil at Re=$2.5*10^5$ for both with and without free stream turbulence. The oil flow technique was used to visualize the flow patterns on the suction surface of the airfoil at different turbulence intensities. He found that increasing the free stream turbulence (FST) from 0.25% to 9% resulted in an increase in peak lift coefficient of 30% with no measurable change in the slope of the lift coefficient vs angle of attack curve occurred. After that saturation of maximum lift occurred. For the case of drag no appreciable change was noticed. This was explained by the fact that the increased friction was almost balanced by the reduction in form drag due to the delay of separation.

Zingg et al [9] made a critical examination of the use of higher order viscous equations in the computations of airfoil flow fields with a viscid-inviscid interaction scheme. Comparisons were made between experimental data and solutions obtained by boundary layer equations, the second order boundary layer equations and the Navier Stokes equations for flows about symmetric and aft-loaded airfoils. Results were restricted to attached incompressible flow. The normal pressure gradients predicted by the higher order procedures were significant in the trailing edge region. The first order procedure underestimated the boundary layer displacement thick-

ness and momentum thickness on the upper surface near the trailing edge. Higher order terms did not significantly affect lift and moment predictions but led to higher and more accurate predictions of drag. The drag coefficient computed with second order procedure was found to be in good agreement with Navier Stokes prediction procedures.

Osswald et al. [10] made direct numerical simulation (DNS) for the dynamic stall process of NACA 0015 airfoil, using unsteady Navier Stokes equations. The rapid pitch up maneuver of the airfoil was examined at Re=1000 and Re=10000 with particular emphasis being placed on the development and evolution of dynamic stall vortex.

Davoudzadeh et al [11] made a two dimensional Navier Stokes study with a finite difference method for the unsteady flow in a linear cascade of J-79 stator blades. Mixing length model was used to account for the effects of turbulence. These studies focussed on the stall inception portion of the overall rotating stall problems for Reynolds number $0.6*10^6$. Three types of calculations were made. The aim of the last set of calculation was to determine the conditions under which a temporarily applied disturbance could lead to self sustaining propagating stall. Calculations were performed at various swirl angles by first obtaining an asymptotic solution at that angle. A wall jet disturbance was then introduced on the suction surface of the

second blade. Typically a stall zone appeared that propagated at suitable angles. After sometime the disturbance was removed and the unsteady response of the flow followed. With 40^0 as the stagger angle, 60.5^0 was predicted as the inflow angle at which a temporarily applied disturbance led to self sustaining stall. At little lower inflow angles such as at 60^0, although the applied disturbance produced rotating stall but as the disturbance was removed the flow returned to its original state.

Jonnavithula et al [12] made a numerical study of stall propagation in axial compressors. In the numerical study compressor blades were represented as an isolated linear cascade of airfoils and stall propagation was simulated using vortex tracking method. The method involved the use of periodic vortex arrays to simulate infinite cascade. The separation point was determined using a boundary layer subroutine and vortex were shed downstream of it. Detailed parametric studies were performed to analyze the effects of flow parameters such as inflow angle, stall wavelength and the geometric parameters such as cascade solidity, blade camber and stagger. Super computer facilities were used for computations. Experimental investigations were conducted in a single stage axial compressor test rig. It was shown that rotating stall had a complex dependence on many parameters such as the relative inflow angle, cascade stagger and stall width. The stall propagation velocity computed, decreased with inflow angle at low stagger angle but increased at higher stagger angle. This also increased with the blade solidity and stall cell wavelength. Exper-

imental results indicated that computational predictions were qualitatively correct. The inaccuracies were attributed to three dimensional effects.

Mitcheltree et al. [13] made a computational study with one equation turbulence model. Length was specified algebraically. Kinetic energy of turbulence was modelled using a transport equation. The flow was studied in the transonic region. Results obtained for both attached and separated flow around NACA 0012 and RAE 2822 airfoils were compared with the Baldwin Lomax model, the q-w two equation turbulence model, the Johnson-King model and available pressure and skin friction data. Based on the results they obtained, they stated that model duplicated the success of algebraic models in attached flow case. For separated flow cases they predicted the shock location and its strength closer to the experimentally observed values than those obtained from both the Algebraic Stress and Two Equation models. However the model suffered the limitation in predicting the shock location for transonic case with large induced separation.

Kandil and Chuang [14] made computations of steady and unsteady transonic flow passing over the NACA 0012 airfoil. For unsteady flow, the airfoil was set in pitching oscillations about a small and moderate mean angle of attack at large amplitude. The results were found to be in good agreement with experimental data with the exception of range of higher angles of attack where the inviscid Eulerian

equations could not handle the smooth surface separation. For unsteady flow, the use of small time steps slightly improved the shock prediction, but this did not change the normal force or pitching moment coefficient.

Mathioudakis and Breugelmans [15] made measurements of three dimensional flow field within a single stage compressor operating in deep rotating stall. A triple hot wire was designed in order to measure the three dimensional unsteady flow. The conclusions made were as follows. The overall features of big stall cells characterized by return flows with high tangential velocity upstream of the rotor and slowly moving flow behind it were confirmed. Radial velocities in the cells were found to be much smaller than the axial and circumferential components. The data proved that unstalled flow did not cross the stall cells in the gap between the blade rows. A succession of flow patterns in a rotor blade passage when it crossed the cell was suggested. Flow was characterized by the presence of two recirculation regions, one being at the rear and one at the front of the blade.

Basuki and Graham [16] used a mixed Eulerian-Lagrangian approach in which discrete vortices were tracked through a grid on which velocity was computed by a finite difference method. Flow past an airfoil with 30^0 incidence was analyzed. The method predicted too strong a roll up of the trailing edge vortex sheet that led to an unrealistic suction peak on the rear upper surface and excessively large

fluctuations in lift. Later, they considered vortex decay technique that led to more realistic results.

Nakahashi et al [17] described a self adapted grid method that was suitable for multidimensional and unsteady computations around airfoils. The method was based on variational principles. Operator splitting , one sided control for orthogonality and smoothness were used to make the method practical, robust and efficient. They described examples for both steady and unsteady viscous flow computations about airfoils in two dimensions. Examples demonstrated a significant improvement in accuracy and quality of the solution. They stated that adaptive grid permitted a more precise description of shock waves and separated shear layers.

Shida et al. [18] made computation of dynamic stall of a NACA 0012 airfoil using two dimensional compressible equations. The block pentadiagonal scheme based on the approximate factorization method was adopted. For a mesh of 321*80, lift stall and restoration of the lift coefficient on the downstroke were captured.

Speziale et al. [19] conducted a numerical simulation of stall propagation in a linear cascade of airfoils at high Reynolds number ($Re=1.0 * 10^7$) using a vortex method. Vorticity was discretized into a large collection of vortex blobs whose motion was tracked in time. Near wall effects of viscosity were accounted for by the

creation of discrete vortex sheets at the boundaries of the airfoils. Detailed computations were conducted over a variety of cascades where the effects of camber and imposed wavelength were studied. An effort was made to parametrize the physical effects of propagating stall through the introduction of mass flow and drag and lift coefficient diagrams. It was found that the range of angles of attack wherein rotating stall occurred was narrower than found in practice. The reason for this was attributed to the fact that the period of cascade was imposed by the numerical method whereas in a real compressor flow field was free to adjust itself to the appropriate wavelength which was physically consistent with other flow parameters. Effects of camber on the range of angles creating propagating stall was found to be significant.

Schafer et al. [20] computed the flow field for a variety of laminar/ turbulent, attached/separated flows through plane cascades. Thin layer and full Navier Stokes equations were solved in 2D and quasi 2D/3D while taking into account variable axial velocity density ratio and cascade aspect ratio. Turbulence was modelled using the Baldwin Lomax algebraic two layer eddy viscosity approach. Improved mesh generation and discretization techniques were introduced. Fully implicit formulation of the problem was developed to ensure high stability and convergence. Numerous quantitative comparisons of viscous solutions with experiments and other existing solutions were performed to validate the numerical code developed. Their prelim-

inary results indicated that thin layer assumptions seemed to be inadequate for accurate computation of separated flows of moderate Reynolds number.

Weinberg et al. [21] made calculations of two and three dimensional transonic cascade flow fields using compressible time dependent Reynolds averaged Navier Stokes equations with k-ϵ turbulence model closure. Three cascade configurations were studied. The calculations predicted most of the known features of the turbine cascade flow fields. These included the flow turning, leading edge stagnation region, boundary layer development, wake development, film cooling effects and three dimensional boundary layer separation were all clearly observed. Converged solutions were obtained within 80 to 150 time steps. The computed heat transfer results indicated a good agreement with the data when an empirical transition model was used. However further work on the laminar turbulent transition models was suggested.

Hah [22] predicted the properties of turbulent flows through a cascade of NACA 65-(18) 10 airfoils at stall conditions. The numerical scheme was based on the fully conservative control volume representation of Navier Stokes equations and solved the equations in elliptic form. Two different turbulence models were used and compared for the effects of streamline curvature for Reynolds number of $2.45 * 10^5$. For non-separated flows accurate predictions for static pressure distribution and turning angles were obtained for both turbulence models. He showed that for flow at stall

conditions, the size of separated flow region was sensitive to the turbulence model used and second model predicted this better. At higher angles of attack, the numerical results indicated slight under-turning of the flow as compared to measurement. The drag coefficient is sensitive to under-turning and hence large deviations between computed and measured values of drag coefficient were found. However the overall agreement for lift coefficient was reasonably good. As a whole second model was found to posses better predicting capabilities.

Paterson and Weingold [23] made an experimental study to predict the flow behavior around the blunt trailing edge airfoil. The objective was to provide the data that could be used to assist the development of computational procedures for predicting such flows. A large scale wind tunnel simulation of trailing edge flow field was made at low Mach number using a flat plate model and laser doppler velocity meter. They found that trailing edge surface pressures and wake static pressures were strongly influenced by the presence of vortex shedding from the plate trailing edge. Viscous induced velocity profile alterations were confined to a region near wake center line having a thickness comparable to trailing edge. Over ten axial chord extent of the recirculation region the outer flow acted as basically inviscid one. They found that the axial extent of the reversed flow region downstream of the trailing edge was approximately eight tenth of the plate thickness.

Berger et al. [24] presented a method of adaptive grid refinement for the solution of steady Euler equations for transonic flow. The boundary conditions required on the fine grid were examined and the importance of treating the fine/coarse grid interface conservatively, was discussed. Numerical results indicated that substantial computational savings could be achieved for the same solution accuracy.

Cross and Denton [25] made an experimental and numerical study for the transonic flow around NACA 0010-34 airfoil. They used an inviscid time marching method. The scheme predicted the flow properties around the leading edge of the blade with high resolution. The agreement was found to be reasonable on the remaining part of the upper surface of the blade including the trailing edge region. The optical system used for the measurements was Holographic interferometer. The advantage of it on other techniques was that typical spacing between interferrometric fringes around the leading edge was 50 μm compared with pressure tapping holes of 200 μm or laser anemometer measurement of 300-500 μm. Information on flow fields in stall cells has been also provided by Das and Jiang[26].

Mehta et al. [27] obtained experimental results for the separated flow over the NASA GA(w)-1 airfoil having 2% trailing edge thickness. The fully separated flow was examined in terms of surface pressure distribution, skin friction, mean velocity profiles and the boundary layer integral properties. Hot wire anemometers was used

for the measurements. Measurements were obtained for surface boundary layers at different angles of attack ranging from 10.3^0 to 18.4^0 . At low angle of attack (10.3^0) the velocity profiles indicated the presence of intermittent separation at x/c of 0.91. For angle of attack of 14.4^0, fully developed separation was found at downstream of x/c of 0.78.

Shamroth et al. [28] applied a numerical solution procedure for the ensemble averaged compressible time dependent Navier Stokes equations to predict the flow around a cascade of airfoils operating in transonic flow regime. Turbulence was taken into account using the mixing length model. Comparison of results with the experimental data showed good agreement for pressure distribution for both subsonic and supersonic cases. However author indicated that further efforts in the area of turbulence modelling were necessary.

The measurement of velocity and flow direction in stall cells of single and multistage compressors were carried out by Day and Cumpsty [29]. Their results dispelled the idea that the cells were "dead wake" regions, and active flow structures were proposed.

Rhie and Chow [30] applied a finite volume numerical method for the solution of two dimensional incompressible Navier Stokes equations in general curvilinear

coordinates. The method was applied to turbulent flow with and without trailing edge separation. The k-ϵ model was used to describe the turbulent flow process. Laminar sub-layer near the wall was treated using the wall functions. O type grid was used and a numerical algorithm similar to SIMPLE was introduced. Results for NACA 0012 airfoil for attached flows were studied at Re=$2.8*10^6$ and Re=$3.8*10^6$. Results were found to be in good agreement with experiment, except at leading and trailing edges. Separated flow around NACA 4412 airfoil was also analyzed. A fairly good pressure distribution was obtained on the airfoil surface except at the leading edge. Discrepancies were found between the predicted and experimentally determined velocity profiles. These discrepancies were attributed to inadequate turbulence modelling and grid refinement.

2.1 Scope of the work

From the literature review relevant to the present study, it is evident that side by side with experimental work, there is a great emphasis made on the numerical study of the aerodynamics of the turbomachinery. This is on one hand because of the cost effectiveness and wider availability of high speed computers and on the other hand to the fact that a numerical solution provides more detailed information about the flow field as compared to the experimental observations. In experimental work,

number of points at which measurements are taken is very limited because it requires heavy instrumentation. The literature review shows it clearly that even those cases which have already been solved experimentally, are being solved numerically . The purpose is to establish validation of newly developed numerical schemes and computer codes. Nevertheless, it is evident that, for turbulent flows, experimental observations are more accurate than numerical predictions because of the approximations in turbulence modelling.

Two types of flow fields can be noticed to be of major interest to researchers in recent years. One is the transonic flow study at small incidences for isolated single and cascade airfoils and the other is the study of flow fields at lower Mach numbers but at large incidences, i.e. the flow fields with separation. The flow field at small incidences and at low Mach numbers is relatively well understood.

Consequently, in the present study, the numerical simulation of the flow field around isolated single and cascade airfoils using Navier Stokes equations is being accomplished. The flow field at high incidences is being studied. For the isolated cascade we introduce the effects of cascade geometric parameters such as solidity ratio (c/s) and stagger, on the flow field. Flow field around an isolated airfoil is also included to provide a reference for the evaluation of cascade performance. This study is expected to widen our knowledge base. Such information is very essential

and beneficial to the aerodynamic design of turbomachinery. We seek to obtain the incidences at which the onset of separation occurs. An interesting study is also included to predict the effects of nose rotation of the airfoil due to expectations that it may cause a delay to the onset of the separation and produce an increase in the lift and a decrease in the drag. For all the cases studied, lift, drag and pressure coefficients are determined, since they are indicative of the performance of the airfoils.

To accomplish this task, we use the control volume method. In this method, the equations are discretized into algebraic equations by performing the integration of the Navier Stokes equations across a finite control volume. These equations are then solved using the Semi Implicit Method for Pressure Linked Equations (SIMPLE) which is an iterative method. The k-ϵ model is being used to take into account the effects of the turbulence. Computational grids are being generated using the algebraic equations for boundary point distribution while the Laplace equation is employed for internal point distribution. A well developed finite volume code (PHOENICS) is being used to accomplish this simulation. PHOENICS stands for "Parabolic, Hyperbolic Or Elliptic Numerical Integration Code". This software has been prepared by CHAM, Wimbledon, London.

Chapter 3

Mathematical Formulation

The physical situations involving fluid flow, mass transfer and heat transfer are governed by the conservation principles of mass, momentum and energy. These principles have been derived in the form of partial differential equations. These equations have the general form of a transport equation as described below.

$$\rho\frac{\partial\phi}{\partial t}+\frac{\partial}{\partial x_i}(\rho u_i\phi)=\frac{\partial}{\partial x_i}\left[\frac{\mu}{\mathrm{Pr}}\frac{\partial\phi}{\partial x_i}\right]+S \tag{3.1}$$

Here ϕ is any transport variable and u is the velocity vector. This equation describes the transport of scaler or vector quantity which takes place because of convection and diffusion processes.

The first term in the general transport equation is called the transient term. It represents the accumulation of variable ϕ in the control volume. The second term is called convection term. This represents the transport of property ϕ due to mass flow in the control volume. The third term is called diffusion. This represents the flow of property ϕ due to its gradient in the flow field. The fourth term is called source term. This represents the rate of generation of the transport variable ϕ within the control volume.

The equations renders a great convenience from the point of view of solution methodology. A computer program which seeks to solve this equation is actually able to simulate transport of any variable by merely changing the Prandtl number and the source term. For example if Pr=1 and S=$\frac{\partial p}{\partial x_i}$, the above equation describes the momentum equation. If $P_r = \frac{\mu C_p}{k}$ and S=0 the above equation describes energy equation without internal heat generation.

3.1 The Governing equations for the System under Study

The particular form of the general transport equation which governs the system under study is being presented below. It is composed of a continuity and two momentum equations. We are considering that no heat transfer takes place in the system so that energy equation is not required. Further since the flow being considered is at a very low Mach number so we are considering the flow as incompressible. As a result no equation of state is required. With the assumption of steady state flow, we have [31]

Mass Conservation: Continuity equation;

$$\frac{\partial}{\partial x_i}(\rho u_i) = 0 \tag{3.2}$$

Momentum Conservation: Navier-Stokes equation

$$\frac{\partial}{\partial x_i}(\rho u_i u_j) = -\frac{\partial p}{\partial x_j} + \frac{\partial}{\partial x_i}\left[\mu \frac{\partial u_j}{\partial x_i}\right] \tag{3.3}$$

where u_j is the velocity component in the coordinate directions x_j, p is the local pressure, and ρ is the fluid density.

3.2 The consequences of extreamly small scale of turbulence

Most flows which occur in practical applications are turbulent; the term denoting a motion in which an irregular fluctuation is superimposed on the main stream. These fluctuations are so hopelessly complex in their details that they seem inaccessible to mathematical treatment [31]. But on the other hand the resulting mixing motion is very important for the course of flow. This entails that a three dimensional unsteady analysis is necessary even for those turbulent flows whose laminar counterpart are steady and one dimensional: e.g. flow in a straight circular pipe. The main difficulty is that the scale of these fluctuations is several orders of magnitude smaller than the flow domain size. This is also true for the time scale of these fluctuations compared to the time scale of interest. The consequence is that typically of the order of 1000 points are required in each flow direction. It means that of the order of 10^9 points are required to fill the three dimensional space [32]. To add to this, the flow being unsteady requires extremely small time steps.

The computational facilities available at present are far beyond those required for an analysis of this kind. In fact many researchers express the idea that we may never be able to simulate turbulent flows using direct numerical simulation (i.e. using full Navier Stokes Equations without any modelling assumptions about structure

of turbulence). At the same time, it should be clear that Engineers in any case are not interested in these small scale fluctuations. The scale of motion which is of practical significance to them is much higher than that of of these fluctuations, both temporally and spatially.

3.3 The Averaging Procedure

Above discussion leads us in a logical way to the statistical approach to obtain the time averaged behavior of the flow properties.

Using statistical methods, the Navier Stokes equations are averaged over a time scale which is much larger than the time scale of turbulent fluctuations, but sufficiently smaller than the time level of interest. The time average flow properties are much smoother in the spatial as well as temporal domains. The consequences are that to capture the flow, a grid with the enormous number of nodes is no more required. In fact, if the mean flow behavior is not changing with time, then, no time marching is required. With time averaged equations, we require a grid having size of the same order as required by a laminar flow for the same system, and, fortunately this time mean behavior is the one of interest to an engineer.

For time averaging, velocities and pressures are separated into a mean and a fluctuating part. The time averaged equations are described below [31].

Mass conservation: (Continuity Equation)

$$\frac{\partial}{\partial x_i}(\rho\overline{u_i}) = 0 \tag{3.4}$$

Momentum Conservation: (Navier-Stokes Equations)

$$\frac{\partial}{\partial x_i}(\rho\overline{u_i u_j}) = -\frac{\partial \overline{p}}{\partial x_j} + \frac{\partial}{\partial x_i}\left(\mu\frac{\partial \overline{u_j}}{\partial x_i}\right) - \frac{\partial}{\partial x_i}(\rho\overline{u_i' u_j'}) \tag{3.5}$$

The equations are formally identical with Navier Stokes equations, if velocities and pressures are replaced by their time averages except for some additional terms, which depend on the turbulent fluctuations of the flow. These terms have appeared as a consequence of the averaging process.

3.4 The Problem of Closure

The above equations, although time averaged, are still exact since no assumptions have been introduced in deriving them, but they no longer form a closed set. The

averaging procedure introduces unknown correlations among the fluctuating velocities. These terms have the behavior of additional stresses on the fluid elements and are called Reynolds stresses. In most cases, these are much larger than their laminar counterpart.

The real difficulty in these equations is that the relationship between the mean and turbulent components is not known. The determination of these correlations is the main problem in calculating the turbulent flow properties. Exact transport equations can be described for these turbulent stresses, but they contain correlations of the next higher order. Their closure is, therefore, not possible in an exact way [32]. Hence, turbulent flows can not be simulated in an exact way using time-averaged equations. We need to make some modelling assumptions about these correlations so as to close our mathematical model. Different modelling assumptions have been proposed for these correlations. These modelling assumptions are called turbulence models. These turbulence models approximate these correlations in terms of mean flow quantities and some empirical constants.

3.5 Order of Turbulence models

If modelling assumptions are introduced for the Reynolds stresses appearing in the time mean equations then turbulence model is known as 'First Order Turbulence Model' [33].

If, however, exact transport equations are introduced for these apparent stresses, then they will contain turbulent correlations of the next higher order. If modelling assumptions are introduced for these correlations, then model is known as 'Second Order Turbulence Model' [33]. With appropriate modelling assumptions and empirical constants these models are much more general and become widely applicable as compared to first order models.

Similarly, higher turbulence models can still be developed which, with appropriate modelling assumptions and empirical inputs, are expected to work better than lower order models.

However, there is a serious problem in this regard. The advantage of higher order models are offset by the fact that number of differential equations comprising the turbulence model increases with the order of turbulence model. The consequences are two fold. Firstly, there is a great increase in the computational effort to solve

the problem. Secondly, and far more serious, is that they require a greater number of empirical inputs and modelling assumptions and, thus, demand great effort to determine the suitable ones. In fact, with poor modelling assumptions and empirical information they can work even poorer than first order models.

For these reasons, to our knowledge, models having an order higher than second order have not been used yet. Great majority of problems is solved using first order models which have so far been reasonably developed and provide satisfactory solution for many problems.

3.6 First Order models

3.6.1 The Boussinesq approximation

Perhaps the first move towards a model of turbulence can be attributed to Boussinesq. All first order models are based on his approximation. He suggested that Reynolds stresses can be expressed in terms of mean flow properties using eddy viscosity concept [33].

Boussinesq approximation:

$$\tau_{ij} = \rho\overline{u_i'u_j'} = \mu_t[\frac{\partial\overline{u_j}}{\partial x_i} + \frac{\partial\overline{u_i}}{\partial x_j} - 2/3(\nabla.\overline{u})\delta_i j] - 2/3\rho k\delta_i j \tag{3.6}$$

Here μ_t is the turbulent eddy viscosity. It is to be noted that μ_t is not a property of the fluid, but it is a function of the local state of turbulence. With this approximation being introduced, the time averaged equations take the following form.

Mass conservation: (Continuity Equation)

$$\frac{\partial}{\partial x_i}(\rho\overline{u_i}) = 0 \tag{3.7}$$

Momentum Conservation: (Navier-Stokes Equations)

$$\frac{\partial}{\partial x_i}(\rho\overline{u_i u_j}) = -\frac{\partial\overline{p}}{\partial x_j} + \frac{\partial}{\partial x_i}\left[(\mu + \mu_t)\frac{\partial\overline{u}_j}{\partial x_i}\right] \tag{3.8}$$

Here the last term of boussinesq approximation has been included in the pressure term, since it represents the normal stress.

Now there remains the task of determining μ_t. Many equations have been proposed to determine it. We will describe them briefly. First we will describe the

fundamental concept behind those equations.

3.6.2 Fundamental Concept in determining μ_t

All the models which seek to determine μ_t utilize a fundamental concept. They assume an analogy between molecular motion and turbulent motion. The turbulent eddies are thought of as lumps of fluids which like molecules collide and exchange momentum. The kinematic viscosity is proportional to the average velocity of molecules and mean free path between them. Likewise the eddy viscosity is considered proportional to a velocity characterizing the fluctuating motion and a typical length of this motion which Prandtl called the mixing length [34].

$$\mu_t \propto \overline{V}\, L \tag{3.9}$$

The analogy is not complete and objections have been raised by researchers, but still the eddy viscosity has been found to work well in practice, especially for two dimensional boundary layer type flows.

Depending on the number of differential equations comprising the models, first order models can be divided into following types.

1. Zero equation models

2. One equation models

3. Two equation models

We will describe one example of each with particular emphasis on two equation k-ϵ model, since this is the model which has been selected for the purpose of this study.

3.6.3 Zero equation models

These models employ no differential equations. The most popular model of this kind is the Prandtl Mixing length model. In this model, the length scale is determined empirically whereas the characteristic velocity of turbulence is determined from the following algebraic expression.

$$V_t = L* \mid (\frac{\partial u}{\partial y}) \mid \tag{3.10}$$

"L" is called the mixing length. Proportionality constant has been taken to be unity. This model has been found to work with limited accuracy for two dimensional boundary layer flows. It has many advantages and disadvantages.

The advantages are [34] :

1. It is simple and requires no additional differential equation.

2. With good choices of mixing length distribution, the realistic predictions are possible.

3. Enough experience has accumulated.

the disadvantages are :

1. It implies zero effective viscosity and thermal conductivity at zero velocity gradient.

2. It takes no account of process of convection and diffusion.

3.6.4 One equation Models

The state of turbulence at a point is influenced by the state of turbulence at other points in the flow. It means that it is not very suitable to determine the velocity scale of turbulence merely by the local flow properties, as is the case with the mixing length model. Rather, a transport equation should be used in determining the velocity scale so that the net effect of neighboring points due to convection and diffusion can be accounted for. The same is true for the case of length scale of turbulence, whose magnitude varies in the flow.

One equation transport models provide a differential transport equation for one

of the two properties; the velocity scale of turbulence. Still the length scale is determined from empirical data.

A well known one equation model is proposed by Prandtl and is called 'K model'. In this model, the velocity scale is taken to be the square root of turbulence kinetic energy. A differential equation is derived from Navier Stokes equations and the unknown terms appearing in the equations are modelled using appropriate assumptions. The modelled form of this approach is given by

$$\rho U_i \frac{\partial k}{\partial x_i} = \frac{\partial}{\partial x_i}\left[\left(\mu + \frac{\mu_t}{\sigma_k}\right)\frac{\partial k}{\partial x_i}\right] + G - \rho\varepsilon \tag{3.11}$$

Here,

$$k = \Sigma u_i'^2 \tag{3.12}$$

and

$$\mu_t = \rho k L \tag{3.13}$$

This type of models has not gained popularity, because there is no transport equation for the length scale and empirical determination of length scale is difficult.

Hence, the advantage of a transport equation for velocity scale is offset.

To obtain the level of generality, especially seeking for recirculating flows we must search the model in which transport effects on the turbulence length scale are also accounted for.

3.6.5 Two equation models

The simplest models for calculating the turbulent complex flows are two equation models employing an additional transport equation for the length scale. Among them the k-ϵ model has been tested most widely and has been shown to predict with the same empirical input, many different flows, including separation and complex three dimensional flows with an accuracy sufficient for practical purposes [35]. This model has all the desirable attributes required of turbulence models, i.e. width of applicability, accuracy, economy of computation and simplicity. Because of these distinguishing features we are employing this model in the present study.

In this model the differential equation for velocity scale is the same as for the "K model". The length scale is determined indirectly, i.e. a differential transport equation is derived for the dissipation of turbulence kinetic energy from Navier Stokes equations. This equation implicitly posseses the length scale. Modelling

C_μ	$C_{\varepsilon 1}$	$C_{\varepsilon 2}$	σ_k	σ_ε	f_μ	f_1	f_2	E'
0.09	1.44	1.92	1.0	1.3	1.0	1.0	1.0	0.0

Table 3.1: Constants for $k-\varepsilon$ model

assumptions are made for the unknown terms appearing in this equation. The complete model is as described below.

$$\rho u_i \frac{\partial k}{\partial x_i} = \frac{\partial}{\partial x_i}\left[\left(\mu + \frac{\mu_t}{\sigma_k}\right)\frac{\partial k}{\partial x_i}\right] + G - \rho\varepsilon \tag{3.14}$$

The isotropic dissipation rate of the turbulent kinetic energy is given by ;

$$\rho u_i \frac{\partial \varepsilon}{\partial x_i} = \frac{\partial}{\partial x_i}\left[\left(\mu + \frac{\mu_t}{\sigma_\varepsilon}\right)\frac{\partial \varepsilon}{\partial x_i}\right] + \frac{\varepsilon}{k}(C_{\varepsilon 1} f_1 G - C_{\varepsilon 2} f_2 \rho\varepsilon) + E' \tag{3.15}$$

where μ_t is called turbulent viscosity and is given by;

μ_t = turbulent viscosity. $C_\mu f_\mu \rho \frac{k^2}{\varepsilon}$

Second last term in equation (3.15), $\rho\varepsilon$ is the destruction rate and G is the rate of generation of turbulent kinetic energy and is given by;

$$G = \mu_t\left[\left(\frac{\partial u_i}{\partial x_j} + \frac{\partial u_j}{\partial x_i}\right)\frac{\partial u_i}{\partial x_j}\right] \tag{3.16}$$

3.7 Law of the Wall

In the very vicinity of the wall, the variations of the flow parameters are so sharp that an extreamly fine grid is required to capture the phenomena accurately and keep the discretization errors within acceptable limits. However, fortunately, there is available an empirically based law that can be used directly to determine the flow parameters in the very vicinity of the wall without having any grid points there. This is called the law of the wall.

From a large amount of experimental data, it has been determined that at a point P near a wall which is at a distance y_p from the wall, the flow velocity u_p is given by

$$u_p = \frac{u^*}{\kappa} \ln(E y_p^+) \tag{3.17}$$

Here u^* is called the friction velocity, and y_p^+ represents the dimensionless distance from P to the wall and;

$$u^* = \sqrt{\frac{T_w}{\rho}} \tag{3.18}$$

$$y_p^+ = \frac{\rho y_p u^*}{\mu} \tag{3.19}$$

Here κ is the Von karman constant and its value is 0.435. T_w is the shear stress at the wall. E is a roughness parameter and its value is taken to be 9 for smooth walls.

It should be noted that this law is applicable when y_p^+ has a value greater than 11.63 . If the distance is less than this value, then point P is in the laminar sublayer so there will be no need of any empirical information for the velocity at point P and Navier Stokes equations can be solved for velocity with the eddy viscosity being set to zero.

We now suppose that the turbulent sublayer is in local equilibrium which means that the rate of production of turbulent kinetic energy is equal to its dissipation rate. Hence the differential equation for k reduces to

$$\frac{\mu_t}{\rho}(\frac{\partial u}{\partial y})^2 = \epsilon \tag{3.20}$$

Using the fact that shear stress at point P in the turbulent layer is approximately equal to the wall shear stress, we obtain

$$\epsilon = \frac{\mu_t}{\rho}(\frac{\partial u}{\partial y}).\frac{\partial u}{\partial y} = \frac{T_w}{\rho}(\frac{\partial u}{\partial y}) \tag{3.21}$$

$$\epsilon = u^{*2}(\frac{\partial u}{\partial y}) \qquad [\text{since } u^* = \sqrt{\frac{T_w}{\rho}}\,] \tag{3.22}$$

Now from Prandtl Kolmogorov law

$$\nu_t = c_\mu \frac{k^2}{\epsilon} \tag{3.23}$$

$$k = \sqrt{\frac{\nu_t \epsilon}{c_\mu}} \tag{3.24}$$

Substituting value of ϵ from equation (3.22) in the above equation yields

$$k = \sqrt{\frac{1}{c_\mu}}\ \sqrt{\frac{\mu_t}{\rho}.u^{*2}.(\frac{\partial u}{\partial y})} \tag{3.25}$$

$$k = \sqrt{\frac{1}{c_\mu}}\ \sqrt{\frac{T_w}{\rho}u^{*2}} \qquad [\text{since } \mu_t \frac{\partial u}{\partial y} = T_w] \tag{3.26}$$

Hence:

$$k = \sqrt{\frac{u^{*4}}{c_\mu}} \qquad [\text{since } \frac{T_w}{\rho} = u^{*2}] \tag{3.27}$$

This expression is used as the boundary condition for k. Now, Differentiating equation (3.17) with respect to y

$$\frac{\partial u}{\partial y} = \frac{u^*}{k}\frac{1}{Ey_p^+}\frac{E\rho u^*}{\mu} \tag{3.28}$$

so

$$\epsilon = u^{*2}\frac{u^{*2}\rho}{k\mu y_p^+} \tag{3.29}$$

$$\epsilon = \frac{u^{*4}}{ky_p u^*} \qquad [\text{since from equation(3.19)} \ \frac{y_p^+\mu}{\rho} = y_p u^*] \tag{3.30}$$

Therefore:

$$\epsilon = \frac{u^{*3}}{ky_p} \tag{3.31}$$

This expression is used as the boundary condition for ϵ.

To obtain u^* appearing in k and ϵ boundary condition expressions we combine (3.17) and (3.19) to obtain

$$|u_p| = \frac{u^\star}{\kappa} \ln(\frac{E\rho y_p u^\star}{\mu}) \tag{3.32}$$

u_p is known from the solution of momentum equation. It should be noted that k and ϵ have not been specified at the wall in contrast to other variables. It is for the reason that the flow immediately adjacent to the wall is laminar and the concept of eddy viscosity does not apply there, therefore, the k and ϵ values are not required there.

3.8 Boundary Conditions

To solve the governing equations, comprising the mathematical model, boundary conditions are needed at each part of the domain boundary. The problem has been solved in x-z plane.

3.8.1 Inlet

The magnitudes of u and w velocities are specified. The magnitude of resultant velocity is 50m/s. The incoming flow has been considered to be turbulence free. As a result the values of k and ϵ have been taken to be zero. For pressure boundary condition either the value of pressure at a boundary is needed or the value of flow rate perpendiular to the boundary is to be specified [33]. At inlet the incoming flow

rate to the domain is specified.

3.8.2 Outlet

We assume that at the exit boundary, convection of flow variables is much larger than the diffusion so that there is no effect of the downstream values on the upstream flow field. As a result no boundary condition is needed at the exit boundary [33]. For making our assumption strongly valid, we take the exit boundary at so large a distance from the airfoil that there is no circulating flow at the exit boundary.

3.8.3 Solid Walls

No slip boundary condition is imposed at the solid boundary. For turbulence quantities. "Law of the Wall" is used to determine their valuse in the first cell adjacent to the wall. These values serve as boundary conditions for the rest of the domain.

3.8.4 Periodic Boundaries

To simulate the infinite cascade, we make use of periodicity assumption. This means that at the remaining boundaries (East and West boundaries) the flow is symmetrical. That is to say that the flow which leaves the flow domain at west boundary reenters the domain at east boundary. Consequently the flow field becomes contineous in the x direction and no boundary condition is needed. In this way the flow field around a single airfoil simulates infinite cascade.

Chapter 4

Solution to the Mathematical Model

Any numerical method which seeks to determine a numerical solution to a set of differential equations has the following basic steps.

1. Discretization of the differential equations into algebraic equations using approximations for the differential operators.

2. Solution of the algebraic equations by direct or iterative methods.

Numerical methods differ from each other in the method of approximation introduced for the discretization of the differential equations. The second step i.e. solution to the resulting algebraic equations is general for all the numerical methods.

In the past decades finite difference method has been the most popular in Computational Fluid Dynamics. This is based on Taylor series expansion. Finite Element Method which was once restricted to structural analysis is also getting attention of researchers in this field, especially for highly irregular geometries. In recent years, Finite Volume Method receives considerable attention. It is similar to the finite difference method, but it has some features that are said to be akin to Finite Element methods. Finite Volume Method has been shown to be physically more realistic [36]. The software that we are using for the present study employs a finite volume method. Therefore, our discussion will be based on this method.

4.1 The Finite Volume Discretization Method

In this method, the calculation domain is divided into a number of non-overlapping control volumes such that there is one control volume surrounding each grid point. The differential equation is integrated over the control volume. Piecewise profiles expressing the variation of variable ϕ are used to evaluate the required integrals. The result is the discretization equation containing the values of ϕ for a group of grid points. The discretization equation obtained in this manner expresses the conservation principle for the finite control volume just as the differential equation expresses

it for the infinitesimal control volume.

4.2 The Discretization Procedure

As described earlier, partial differential equations are to be discretized into algebraic equations by using appropriate approximation to obtain a numerical solution to the problem. The procedure followed is the Finite Volume Method. It will be described in general curvilinear coordinates for the general transport equation for an orthogonal coordinate system.

In vector notation, the general transport equation for steady state situation is given by

$$\nabla.(\rho \mathbf{U} \phi) = \nabla.(\Gamma_\phi \nabla \phi) + S \tag{4.1}$$

This equation is integrated over the finite control volume around node P, shown in figure (4.1).

We have

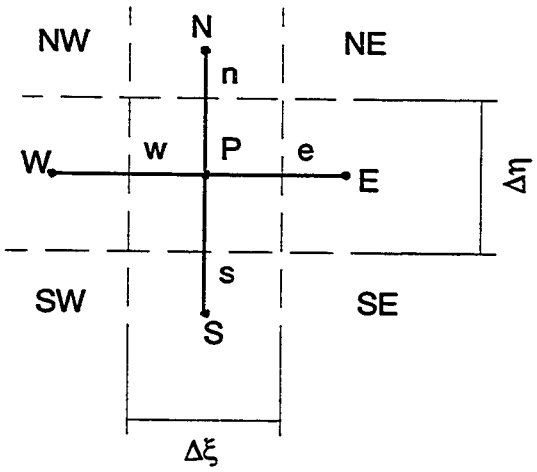

Figure 4.1: A finite control volume

$$\int_s^n \int_w^e [\nabla.(\rho \mathbf{U}\phi)] d\eta d\xi = \int_s^n \int_w^e \nabla.(\Gamma_\phi \nabla\phi) d\eta d\xi + \int_s^n \int_w^e S d\eta d\xi \qquad (4.2)$$

or

$$[(\rho u_\eta \phi - \Gamma_\phi \frac{\partial \phi}{\partial \eta})\Delta\xi]_s^n + [(\rho u_\xi \phi - \Gamma_\phi \frac{\partial \phi}{\partial \xi})\Delta\eta]_w^e = \overline{S}_\phi \Delta\xi\Delta\eta \qquad (4.3)$$

Here $\overline{S}_\phi$ is the average value of S over the finite control volume and u_ξ, u_η are the components of velocity vector U in the orthogonal coordinate directions ξ and η respectively. We represent the total flux across a face of the finite control volume by J for convenience. Focussing our attention on east face

$$J_e = [\rho u_\xi \phi_e - (\Gamma_\phi \frac{\partial \phi}{\partial \xi})_e]\Delta\eta \qquad (4.4)$$

It is clear that total flux is composed of a convective flux and a diffusive flux. We represent them by C_e and D_e respectively.

$$C_e = \rho u_\xi \phi_e \Delta\eta \qquad (4.5)$$

$$D_e = (\Gamma_\phi \frac{\partial \phi}{\partial \xi})_e \qquad (4.6)$$

To get the linear algebraic equations, the source term is appropriately linearized.

$$S_\phi = S_0 + S_p \phi_p \tag{4.7}$$

Hence we have

$$J_e - J_w + J_n - J_s = (S_0 + S_p \phi_p)\Delta\eta\Delta\xi \tag{4.8}$$

To make further progress we need to make profile assumptions about the variation of ϕ within the finite control volume. For the diffusion flux a linear profile can be assumed. This results in the central discretization

$$D_e = (\Gamma_{\phi_e} \frac{\partial \phi}{\partial \xi})_e = \Gamma_{\phi_e} \frac{(\phi_E - \phi_P)}{\Delta\xi_{PE}} \tag{4.9}$$

Central discretization is usually not appropriate for the convective flux and may result in non-physical oscillations in the solution. To make the discretization compatible with physical reality a hybrid scheme is used. Depending on the Cell Peclet number it uses either an upwind or central discretization for the convective flux C_e. Cell Peclet number is defined as

$$P_e = \frac{\rho u_\xi \Delta\xi_{PE}}{\Gamma_{\phi_e}} \tag{4.10}$$

Using Hybrid Scheme

$$C_e = \rho u_\xi \frac{(\phi_E + \phi_P)}{2} \Delta\xi. \quad \text{if } -2 \leq P_e \leq 2 \tag{4.11}$$

$$C_e = \rho u_\xi \phi_E \Delta\xi. \quad \text{if } P_e > 2 \tag{4.12}$$

$$C_e = \rho u_\xi \phi_P \Delta\xi. \quad \text{if } P_e < 2 \tag{4.13}$$

Similar expression are obtained at other faces of the finite control volume. Substituting these expressions in equation 4.8 we get

$$(A_P - S_P)\phi_P = A_n\phi_n + A_s\phi_s + A_e\phi_e + A_w\phi_w + S_0 \tag{4.14}$$

where

$$A_e = \frac{\Gamma_{\phi_e}}{\Delta\xi_{PE}} - \rho u_\xi)_e \tag{4.15}$$

$$A_w = \frac{\Gamma_{\phi_w}}{\Delta\xi_{WP}} - \rho u_\xi)_w \tag{4.16}$$

$$A_n = \frac{\Gamma_{\phi_n}}{\Delta\eta_{PN}} - \rho u_\eta)_n \tag{4.17}$$

$$A_s = \frac{\Gamma_{\phi_s}}{\Delta\eta_{SP}} - \rho u_\eta)_s \tag{4.18}$$

$$A_P = A_e + A_w + A_n + A_s \tag{4.19}$$

Here $u_\xi)_e$ represents u_ξ velocity at the east cell face. In this connection it should be clear that this velocity is not an interpolated one, but rather it is indeed calculated at cell faces in contrast to other variables whose values are calculated at the center of the cells, therefore, at faces the values can be obtained through interpolation. This arrangement is highly beneficial to avoid a non-physical oscillatory solution for the pressure field and to increase the accuracy.

4.3 Grid Generation

For numerical simulation of flow fields around airfoils, three grid types are usually used, namely C type, H type and O type grids [33]. Figure(4.2) shows these types.

C and O type grids have nearly orthogonal cells. H type grid is comparatively much non orthonal. Because of this fact, the convergence rate of iterative solution method is much slower on this grid as compared to C and O type grids. However PHOENICS is yet incapable of using a C-type grid for flow field simulation of airfoil cascades. Hence we made our study on H-type grid.

The grid for the present study was generated using algebraic equations for the boundary nodes and Laplace equation for the interior nodes with an effort to minimize the non-smoothness of the grid, but at the same time having grid clustering at regions of larger gradients to obtain an economic and accurate solution.

The iterative method is sensitive to the smoothness and orthogonality of the mesh generated. For non-smooth meshes, heavy underrelaxation is required to prevent divergence of the solution. This large underrelaxation reduces the convergence rate with the consequence of increased computational effort [37].

4.4 Calculation Procedure

For the general variable ϕ the solution to the discretized algebraic equations can be obtained using either direct or iterative methods. Direct method needs the algebraic equations to be linear. If, however, the equations are nonlinear then an iterative

MESHSIZE : 97• 17

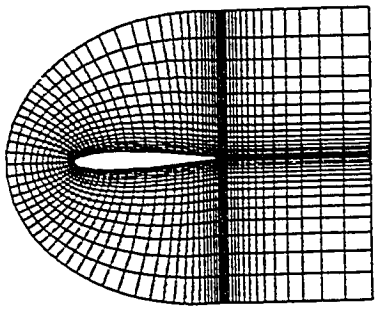

(a) C - mesh

MESHSIZE : 33• 9

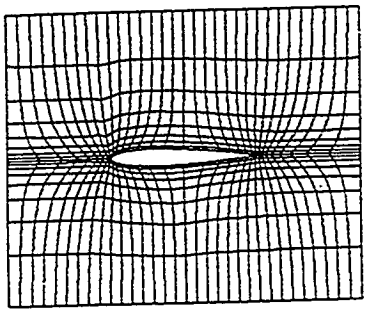

(b) H - mesh

MESHSIZE : 65• 13

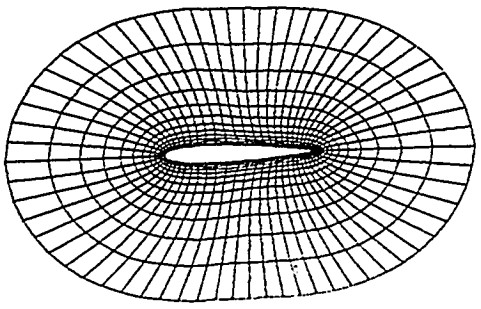

(c) O - mesh

Figure 4.2: Typical grid types (a) C-type (b) H-type (c) O-type

method is necessary. Some of the algebraic equation solvers which PHOENICS possesses are

1. Gauss Siedal Method
2. Whole field solution method
3. Tri Diagonal Matrix Algorithm
4. Multigrid Method

Gauss Siedal method requires the least number of calculations, over the solution domain, per iteration. However, it requires a large number of iterations for convergence, since the boundary information enters the solution domain one node forward every iteration. Whole field is very efficient for linear algebraic equations for a moderate size matrix. It shifts the boundary information inside the flow system immediately, since it solves the equations simultaneously. However if the grid size is large, then matrix size becomes very large, and requires a very large computer memory and enormous computational power [38]. If the algebraic equations are nonlinear, then whole field method has to work iteratively since the coefficients of the discretized equations, being tentative, are to be updated at the end of every sweep using the new values of ϕ, until the convergence is met. Hence, for nonlinear algebraic equations, even for a moderate size of matrix, this method may require

a much larger total computational effort as per required by the Gauss Siedal Method.

A method which has the benefits of both, but disadvantages of none is the Tri Diagonal Matrix Algorithm. In this method, algebraic equations for a row of nodes are solved simultaneously. A very efficient algorithm which is called Thomas Algorithm is available to solve the tridiagonal matrix, thus, formed. Hence, the boundary point information is carried in a single iteration for that row. The solution procedure proceeds to the next column and repeats itself. Therefore, this method works like whole field method in the row wise direction and like Gauss Siedal method in the column wise direction. The number of total computational effort needed is only little greater than Gauss Siedal Method. This is due to the usage of Thomas Algorithm. Most of the time, we used this method for the solution of our problem. However, equation for pressure correction was solved using the whole field method, since a simultaneous satisfaction of the continuity in the whole domain increases the convergence rate. Usually several hundred sweeps are required to obtain a converged solution.

It should be noted that multigrid method is an advanced iterative method and has very high convergence rate. For problems requiring enormous computational effort, it is very attractive. However, for moderate size problems like ours, the more traditional methods suffice. These days it is in the development stage, and a good

account of this method can be found in [39].

4.4.1 The Momentum Equations

If the pressure field is given, the solution to the momentum equations can be obtained by employing the method described above. However, unless the correct pressure is employed, the resulting velocity field obtained from the solution of the momentum equations will not satisfy the continuity equation. However, no explicit equation for the pressure is given. This is particularly true for an incompressible flow. In this regard several methods are available. PHOENICS uses the SIMPLE procedure. This method has been described in detail in the literature [36] and it is basically an iterative process.

Let a tentatively calculated velocity field based on a guessed pressure field p^* is denoted by u_ξ^*, u_η^* and let the correct pressure p be obtained from

$$p = p^* + p' \tag{4.20}$$

The corresponding correction in velocities u'_ξ, u'_η can be introduced in a similar manner

$$u_\xi = u_\xi^* + u'_\xi \tag{4.21}$$

$$u_\eta = u_\eta^* + u'_\eta \tag{4.22}$$

Making certain assumptions, the velocity correction formula for east face of the mesh element, for example, is given by

$$u_\xi = u_\xi^* + \frac{\Delta\eta}{A_c}(p'_P - p'_E) \tag{4.23}$$

Now, discretizing the continuity equation and using the velocity correction formulas, one can obtain an equation for pressure correction

$$(A_P - S_P)p_P = A_n p'_n + A_s p'_s + A_e p'_e + A_w p'_w + S_0 \tag{4.24}$$

Thus we have obtained an equation for pressure correction or in turn for pressure. The important steps to compute the flow properties are as follows.

1. Guess the pressure field p^*.

2. Solve the momentum equations to obtain u_ξ^* and u_η^*.

3. Solve the pressure correction equation.

4. Calculate p by adding p' to p^*.

5. Solve equations for other variables ϕ (e.g. turbulence kinetic energy), if they have a coupling with momentum equations.

6. Treat the corrected pressure as a new guessed pressure p^*. Return to step 2 and repeat the whole procedure until a converged solution is obtained.

Chapter 5

RESULTS AND DISCUSSIONS

The viscous incompressible flow in a cascade of NACA 0012 airfoils is studied at Re=3.24*10^5. The airfoil geometric coordinates have been taken from the reference [40]. An H-type grid has been used. In order to increase the accuracy of the calculations and for economy of computations, a high grid refinement was introduced near the solid boundary. The front and rear outer boundaries are located at 1 and 2 chord distances away from the body respectively. Single passage periodicity assumption was used to simulate the infinite cascade. The iterative method is considered to be converged when the residuals diminish by an order of 4 compared with their initial values. For the parametric study, the angle of attack is varied from 0^0 to 24^0 degrees gradually, solidity(c/s) ranges from 0.55 to 0.83 and stagger angle varies from 10^0 to 30^0.

5.1 Isolated Single Airfoil

Figure (5.1) shows the computational grid for the isolated airfoil. The front and rear outer boundaries are set such that they are at one and two chord distances away from the airfoil respectively. Each of the top and bottom boundaries have been taken at five chord distances away from the airfoil. At these boundaries, the flow is inviscid and has the same velocity as being at inlet.

Figure (5.2) shows the velocity field around the isolated single NACA 0012 airfoil for three different angles of attack. It is obvious that boundary layer thickness is considerably small at the leading edge and increases along the chord. At the upper and lower surfaces of the airfoil, nearly symmetric boundary layer profiles are obtained at an angle of attack (α) of 3^0, as expected. As the angle of attack increases this symmetry disappears and considerable difference occurs. The development of free shear layer at the trailing edge is visible. This free shear layer diminishes in the downstream because of the diffusion process.

Figure (5.3) shows the streamline plots of the flow field . At 3^0 angle of attack, the straemlines show a new nearly symmetrical picture. At 16^0 angle of attack, a big recirculation region appears at the trailing edge. On the suction surface, a reduction in the velocity, accompanied by an increase in the boundary layer thickness, is quite

apparent at the trailing edge at higher angles of attack.

Figure (5.4) shows pressure contours obtained for an isolated single NACA 0012 airfoil for various angles of attack. Stagnation region moves down from the leading edge to the pressure surface of the airfoil as the angle of attack increases. The contours show larger values of pressure on the lower surface of the airfoil as compared to the upper surface. This difference in pressures generates a lift. The contours clearly show that sharp pressure varaitions occur at the leading edge of the airfoil, whereas, at the trailing edge the variations in pressure are much smoother.

Figure(5.5) shows the grid independence test for the simulation of flow field developed around an isolated airfoil. Three different types of grids have ben investigated and it is found that all of the grids result almost the same flow field. Therefore, a grid of 80*90 has been selected in the present study.

Figure (5.6) shows the pressure coefficient along the chord length. At the leading edge an abrupt change in the pressures occurs, followed by a smooth variation along the chord, thereafter. The profile shows clearly that most of the lift that airfoil experiences, is generated at the leading edge and rear part of the airfoil has a small contribution in it. It is evident that following the points of suction and pressure peaks on the suction and pressure surfaces respectively, the pressure surface has a

favorable pressure gradient whereas the suction surface has an adverse pressure gradient. At the trailing edge, pressures on the two surfaces become almost the same. It is noticed that angle of attack has a significant effect on the pressure gradient. As the angle of attack increases, the adverse pressure gradient just after the point of suction peak attains a large value. At high incidences, this gradient becomes so large that separation is resulted.

The pressure coefficients calculated from present study have been compared with the experimental data available [30], [41] and [42]. The agreement between the two results has been found to be good, except at the leading edge where experimental results show a large suction peak. This is attributed to the inaccuracies incurred by the turbulence model approximations. It is to be noted that for comparison, the simulations have been made at the same Reynolds numbers as those of the available experimental data. The rest of the predictions have been made at Re=$3.24*10^5$.

Figure (5.7) shows the lift and drag coefficients of the isolated airfoil. Lift and drag coefficients increase as the angle of attack increases. As the separation appears, a very sharp increase occurs in the drag. Consequently, the lift coefficient is expected to decrease rapidly. However, this is not the case in the present analysis, which may be due to the reason that in the present study, steady state analysis is considered, therefore, the unsteady nature of the separation and its effects are

not taken into account. Once the separation is resulted it remains steady without forming the vortex shedding. The calculated lift and drag coefficients have been compared with the experimental data available [41]. The lift and drag coefficients follow the same trends as those predicted by the experiment. However, the magnitude of predicted lift coefficient is smaller than found in experiment. This may occur due to two reasons. Firstly, because of the approximate nature of numerical integration used to calcualate lift and secondly, because the present simulation did not predict as large a suction peak as it appears in the experiments.

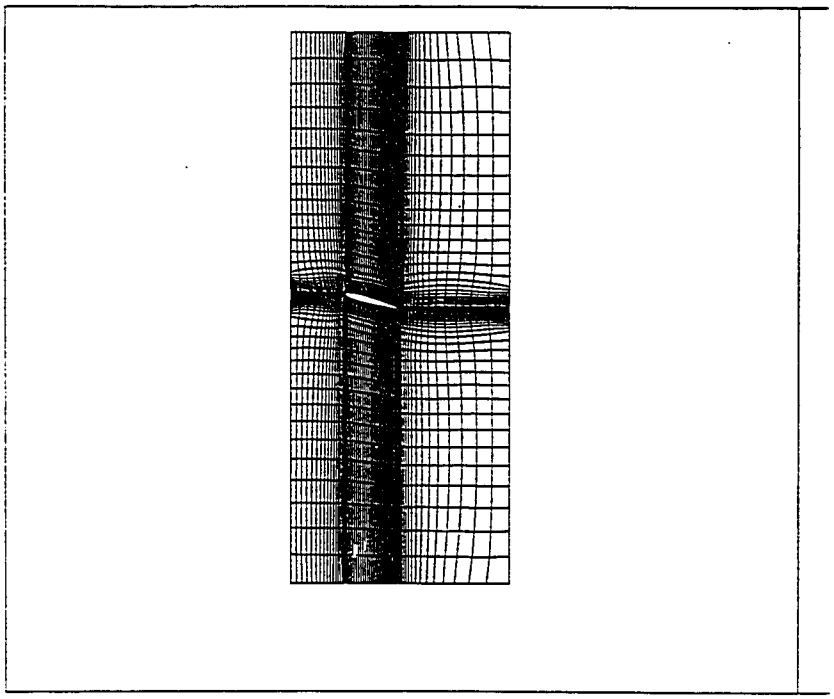

Figure 5.1: 90*80 H-mesh for the isolated airfoil

(a)

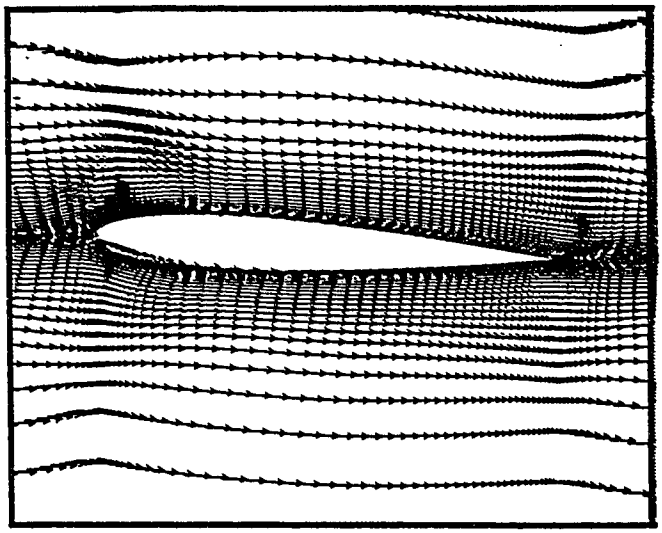

(b)

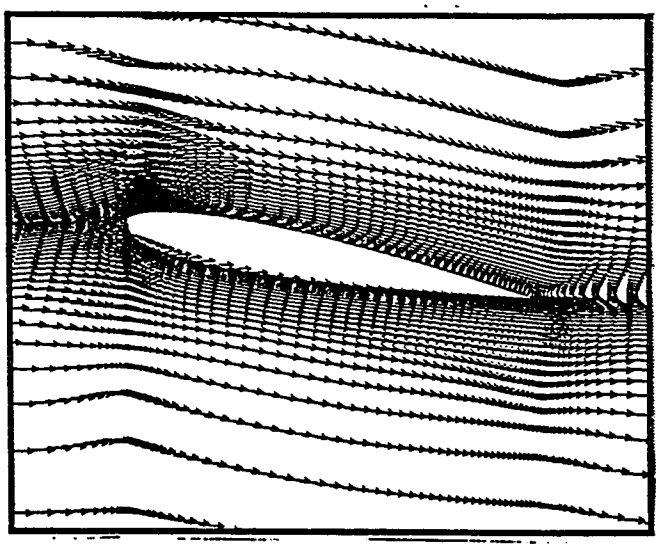

(c)

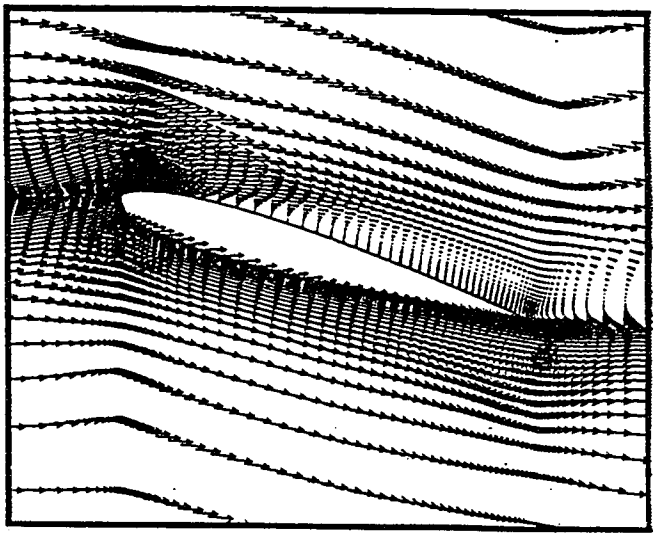

Figure 5.2: Velocity vector fields for the isolated airfoil at different angles of attack (a) 3^0 (b) 10^0 (c) 16^0

(a)

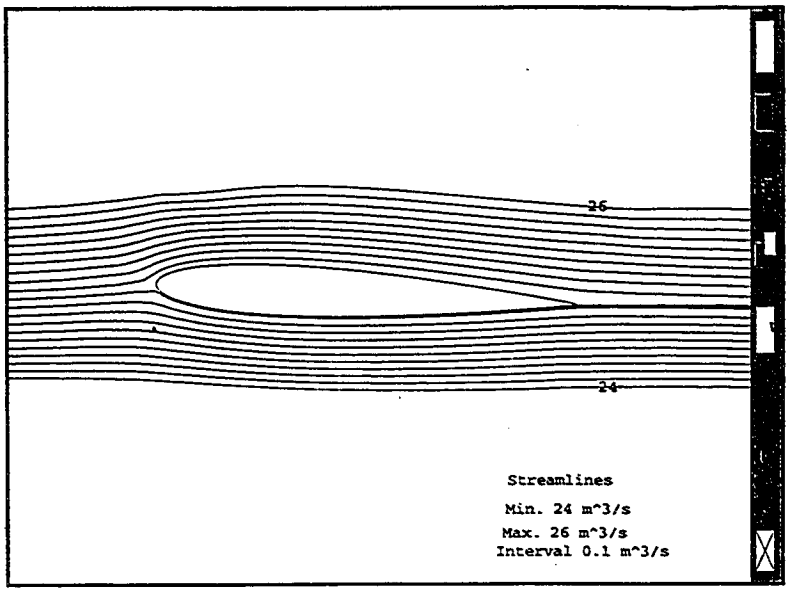

(b)

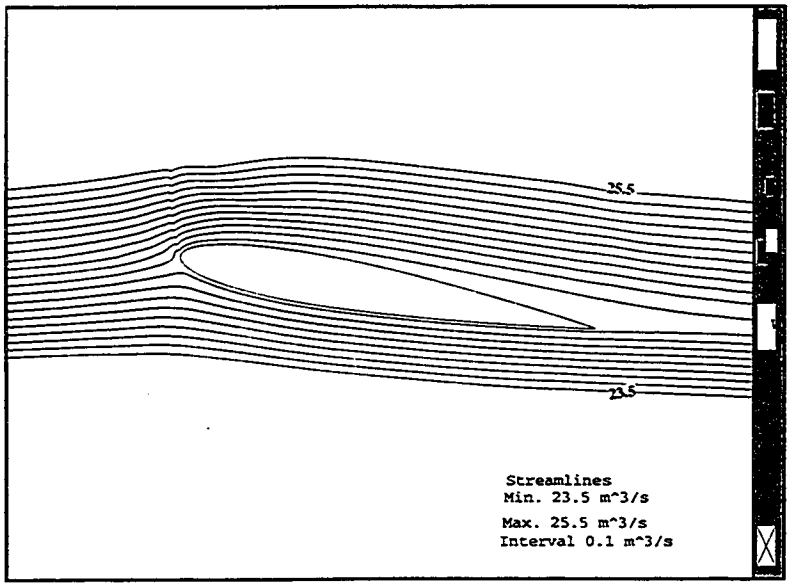

(c)

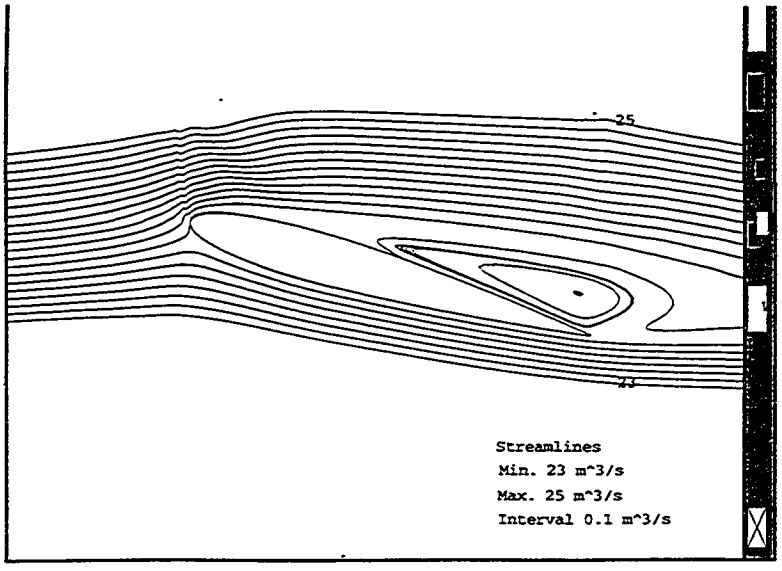

Figure 5.3: Streamline contours for the isolated airfoil at different angles of attack (a) 3^0 (b) 10^0 (c) 16^0

(a)

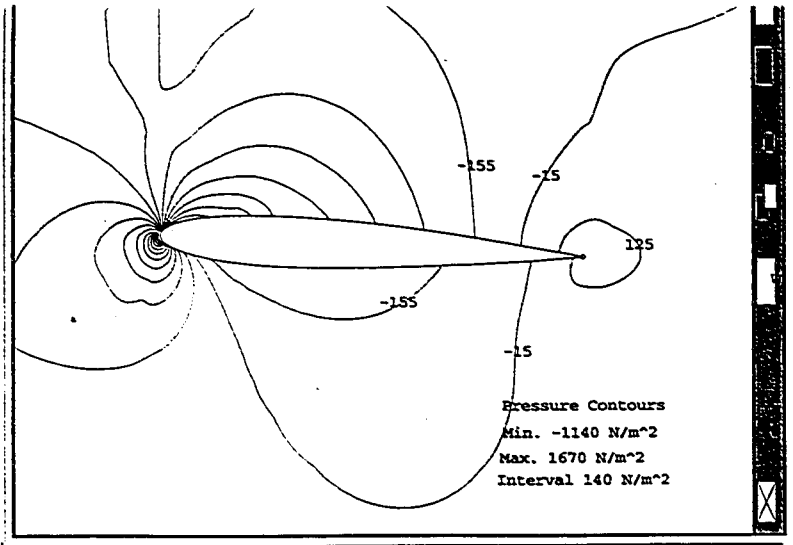

(b)

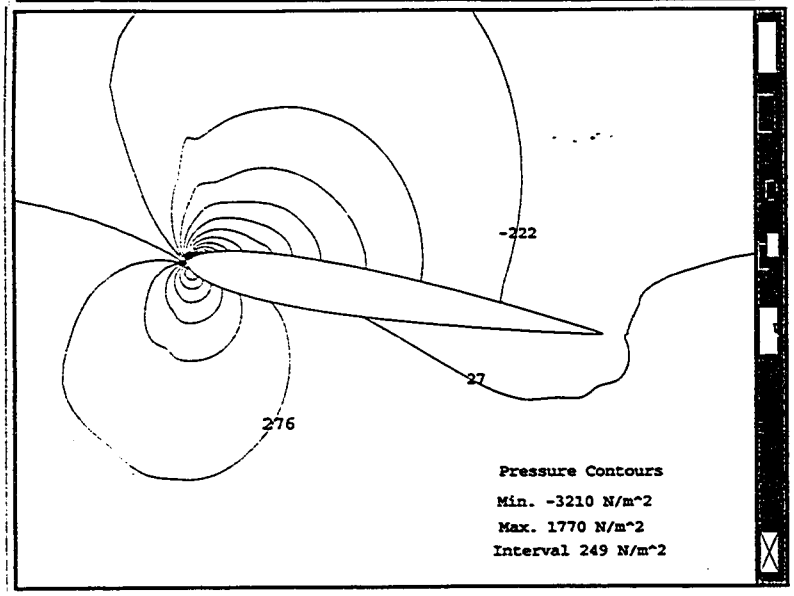

(c)

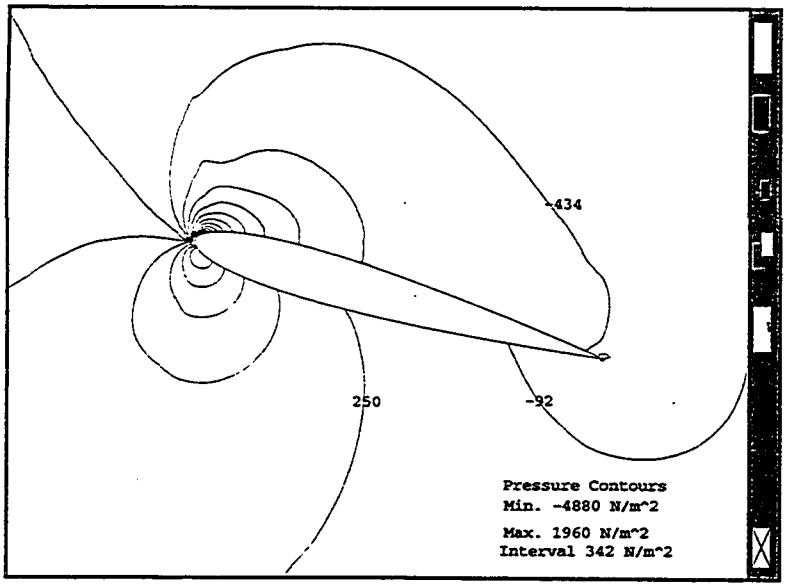

Figure 5.4: Pressure Contours for the isolated airfoil at different angles of attack (a) 3^0 (b) 10^0 (c) 16^0

5.2 Effects of Solidity Ratio

Figure (5.8) shows the 80*60 H-type meshes for two different values of the solidity ratio. The stagger angle is fixed at 30^0. Near the airfoil surface, the grid clustering is almost the same for the two cases to obtain the solutions of similar accuracy. At large distances from the solid body the gradients are expected to be small, hence, large grid clustering is avoided there to save the computational effort.

Figure (5.9) shows the grid independence test for the solution of cascade flow field at c/s of 0.83 and at stagger of 30^0 for an angle of attack of 20^0. In this case, 80*62 and 100*80 size grids have been tested. The results are almost identical. Hence, we have selected 80*62 size grid for our study of cascade flow fields.

Figures (5.10), (5.11) and (5.12) show the flow field around the infinite cascade of NACA 0012 airfoils for c/s of 0.55 and 0.83 respectively . It is evident that increase in the solidity (c/s) effects the boundary layer development around the airfoils. Separation starts earlier in the case of low solidity (c/s).

Figure (5.13) shows the streamline plots of the flow field around the trailing edge at an angle of attack of 22^0. The cascade with a low solidity shows separation, whereas the flow is still attached in the case of the cascade with higher solidity(0.83).

This attachment is due to pressure suppression caused by the influence of the adjacent airfoil. At low solidity this influence reduces with the consequence that the flow can not have a high turning angle and thus separation is resulted.

In all the cases, the flow spilling at the leading edge is obvious. Figure (5.14) shows enlarged views of the spilling and separation processes at 24^0 angle of attack. Due to symmetrical arrangement of airfoils, the separation occurs at all the airfoils for the same angle of attack. The boundary layer thickness increases along the chord and the boundary layer profiles are very similar at low incidences along the chord. At high incidences, these profiles distorted considerably. At separation, the boundary layer has a point of contraflexure, where the slope of the profile changes its sign.

The maximum velocity occurs at the leading edge of the airfoil. This is accompanied by a suction peak. With the increase in solidity, this velocity peak reduces in magnitude, causing a reduction in the suction peak.

Figure (5.15) shows the pressure coefficients along the chord of the cascade for two different solidity ratios and at different angles of attack. The suction peak on the airfoil surface decreases as the solidity increases. As described earlier, this is due to the pressure suppression as a result of closely spaced airfoils in the cascade. It should be noted that isolated single airfoil has the largest suction peak.

Figure (5.16) shows the lift and Drag Coefficients corresponding to different Solidity Ratio. Lift coefficient increases with increasing angle of attack. The maximum obtainable lift becomes small as the solidity increases. This is due to the loss in the suction peak at the upper surface as it is influenced by the high pressure region on the pressure surface of the neighboring airfoil. The angle of attack corresponding to separation point moves to relatively high values as the solidity increases.

Drag coefficient increases as the angle of attack increases and it reduces slightly with the increase in solidity ratio. Isolated airfoil has the largest drag for a given angle of attack. The curves show clearly that as the separation is reached the drag increases sharply, whereas the lift drops.

5.3 The effects of stagger

Previous discussion was limited to the study of the effects of solidity ranging from 0.83 to zero(isolated airfoil). In the present section we will describe the effects of stagger on the performance of the cascade. For this purpose, solidity ratio has been fixed to a value of 0.55 whereas two values of stagger have been chosen for comparison.

It is obvious that an increase in stagger results in an increase in the departure of the grid from the orthogonality. This requires an increase in the underrelaxation to prevent divergence of the iterative solution method and the consequence is a decrease in the convergence rate. It should be noted that it is possible to generate an orthogonal grid by using a Laplace type differential equation, but this orthogonality is obtained at the cost of great non-smoothness in the grid. The grid clustering is not present at the desired regions. Hence, we loose the control of cell sizes and their distribution to fulfil our requirements. Further, this highly non-smooth, although orthogonal, grid is more prone to create a divergence of the solution procedure. For these reasons we use a non-orthogonal smoother grid with a cell distribution to satisfy the convergence requirements. Because of this non-orthogonality, the convergence is slower in the case of high stagger as compared to the cascade with low stagger. For zero degree stagger the convergence is met the earliest.

Figures (5.17), (5.18) and (5.19) show the flow fields obtained for the two cases of stagger at different angles of attack. Figure (5.20) shows streamline plots corresponding to 22^0 angle of attack. The figures show that airfoils at 10^0 stagger have a large flow spilling and hence they have a large peak velocity at various incidences. Downstream of the trailing edge, a free shear layer develops due to the velocity difference of the flow passing through the upper and lower surfaces of the airfoil. This diminishes further in downstream because of the momentum diffusion and the turbulent fluctuations. The velocity distribution is similar around each airfoil in the cascade. It is to be noted that at high incidences, boundary layer thickness is significant at the trailing edge. This shows that it could not be wise to use the viscid-inviscid interactive method for the present study and the full Navier Stokes solution becomes necessary. A good account of interactive methods for airfoil calculations has been presented in [43]. At 22^0 angle of attack, the flow corresponding to 30^0 staggered cascade airfoils detaches from the surfaces. Whereas, for 10^0 staggered cascade airfoils, the flow is still attached at this angle of attack. This is because of the high flow velocity occurring at the leading edge. In this case, the momentum is large enough to overcome the adverse pressure gradient.

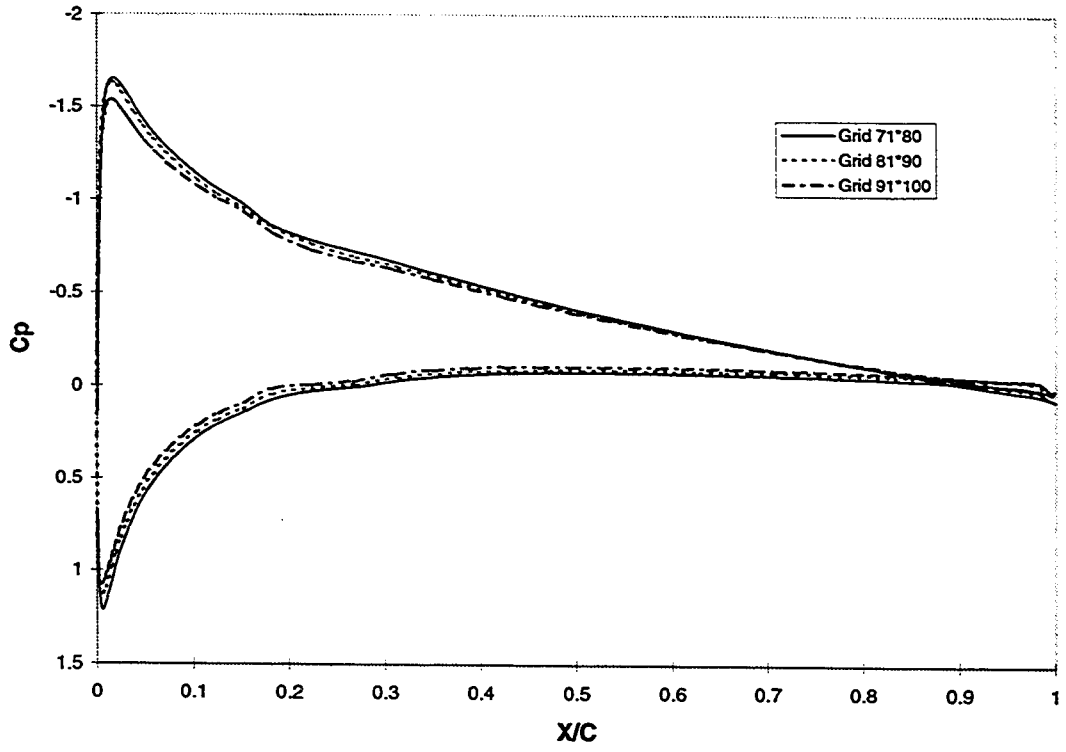

Figure 5.5: Surface Mean Pressure Coefficients for the isolated airfoil for three different grid arrangements at $\alpha = 7.5^0$

(a)

(b)

(c)

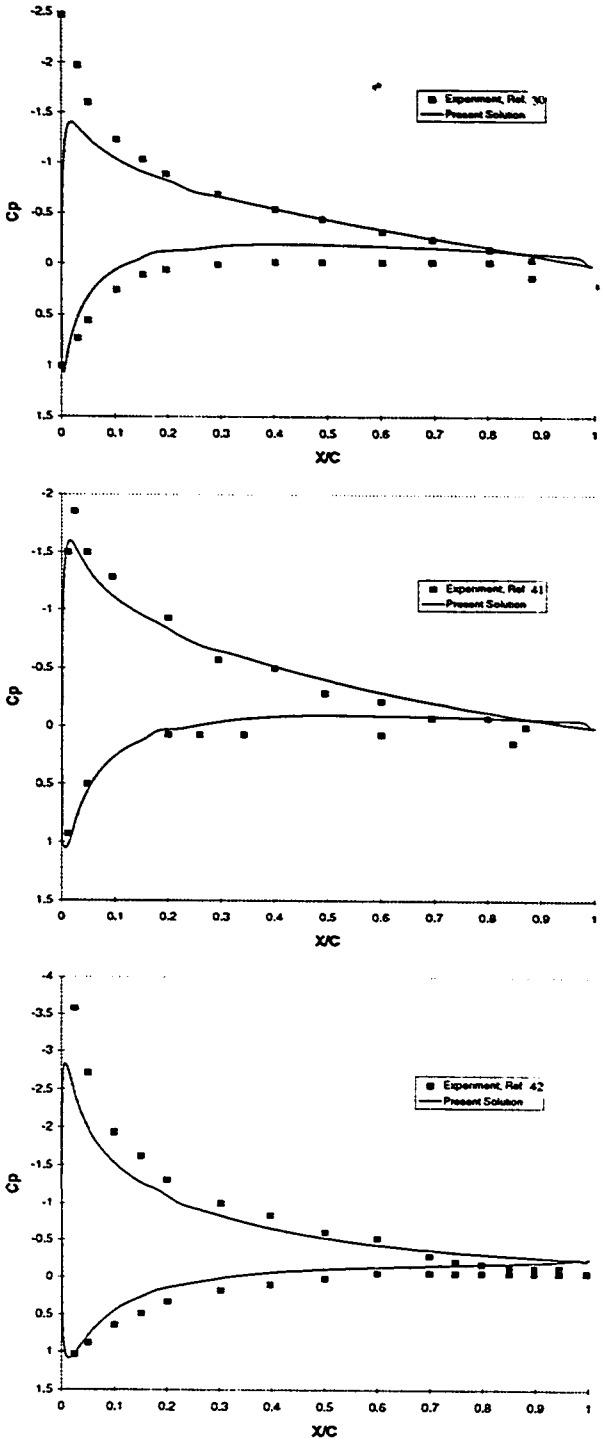

Figure 5.6: Surface mean pressure coefficients for the isolated airfoil at different angles of attack (a) 6^0 (b) 7.5^0 (c) 12^0

(a)

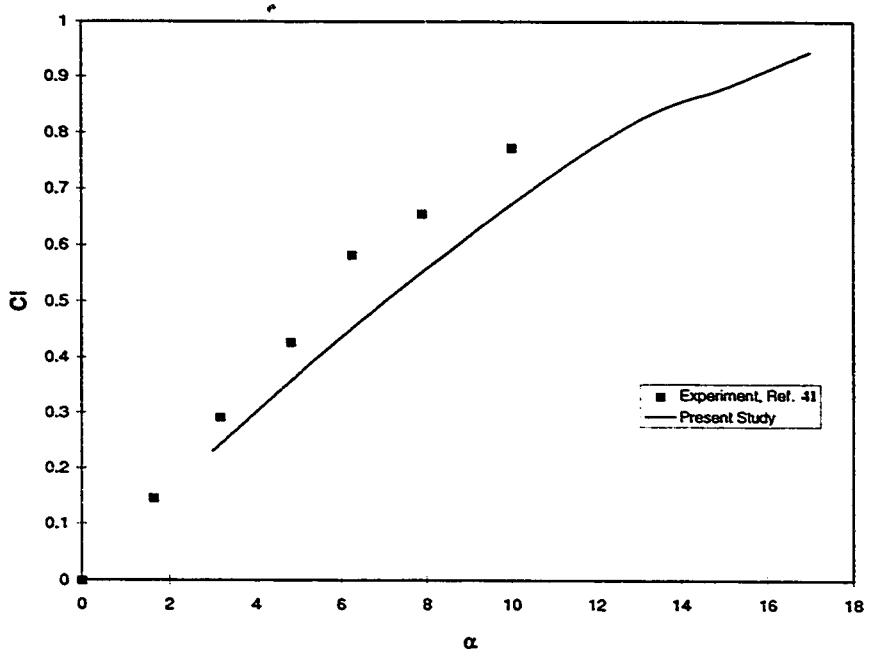

(b)

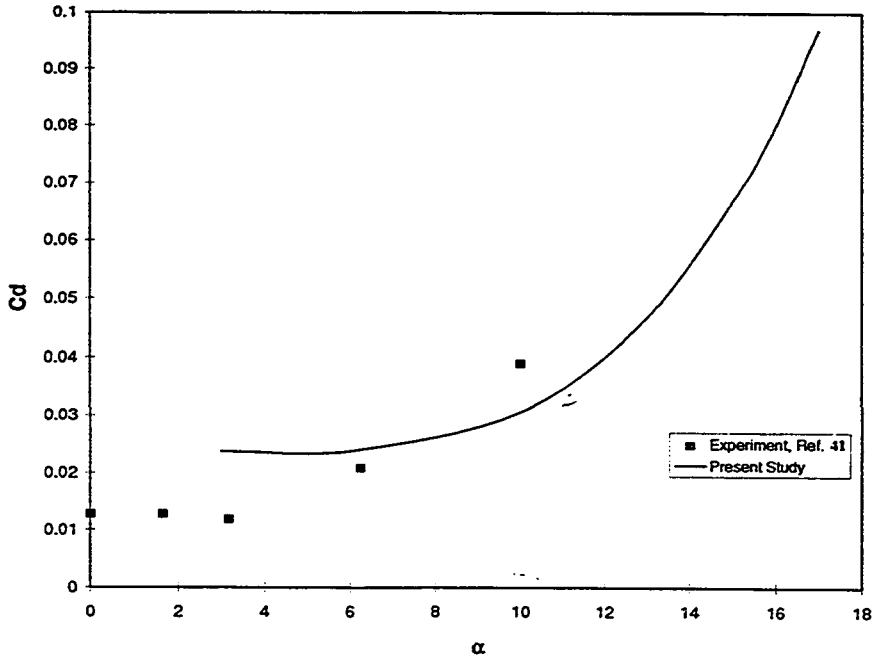

Figure 5.7: (a) Lift Coefficient (b) Drag Coefficient for the isolated airfoil

(a)

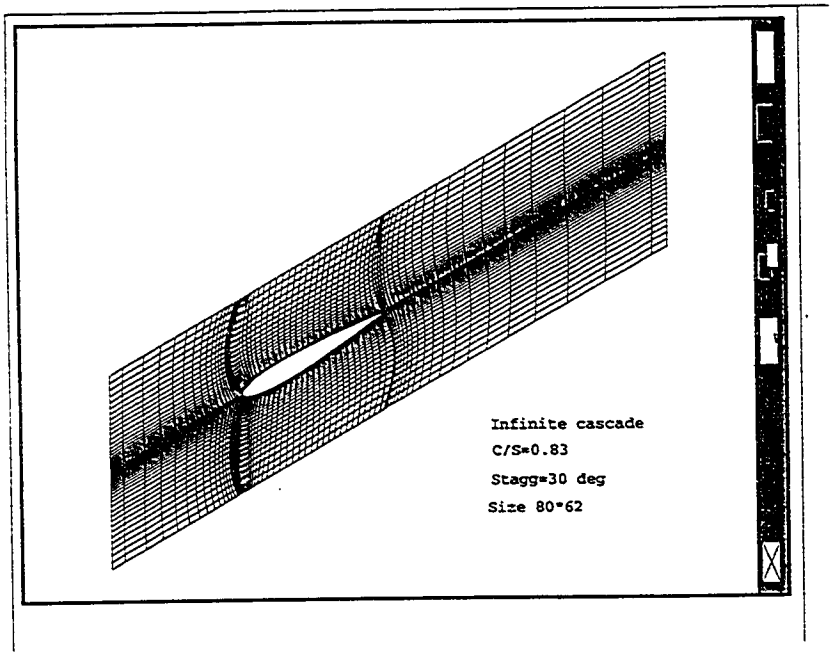

(b)

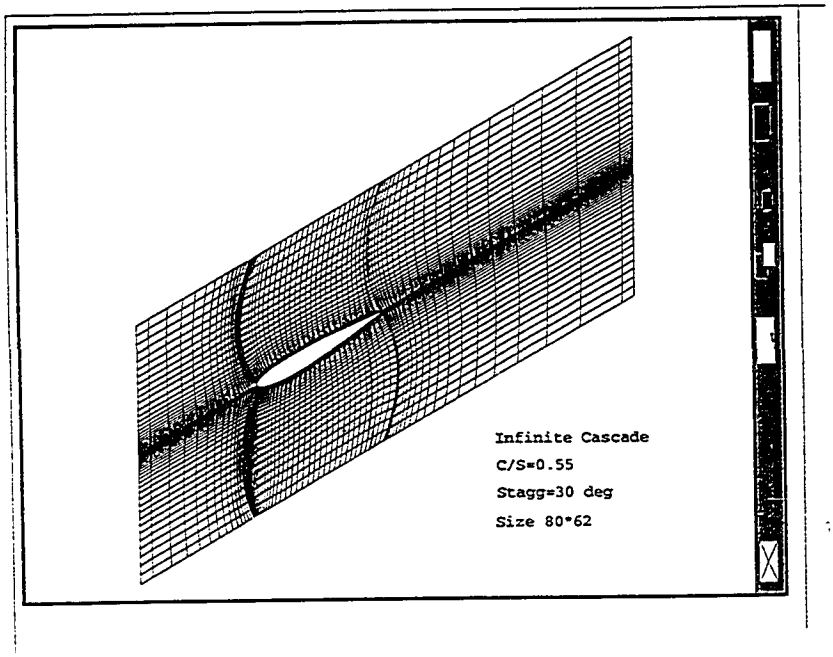

Figure 5.8: Mesh Arrangements for the infinite cascade, Stagger=30^0, at different solidity ratios (a) C/S=0.83 (b) C/S=0.55

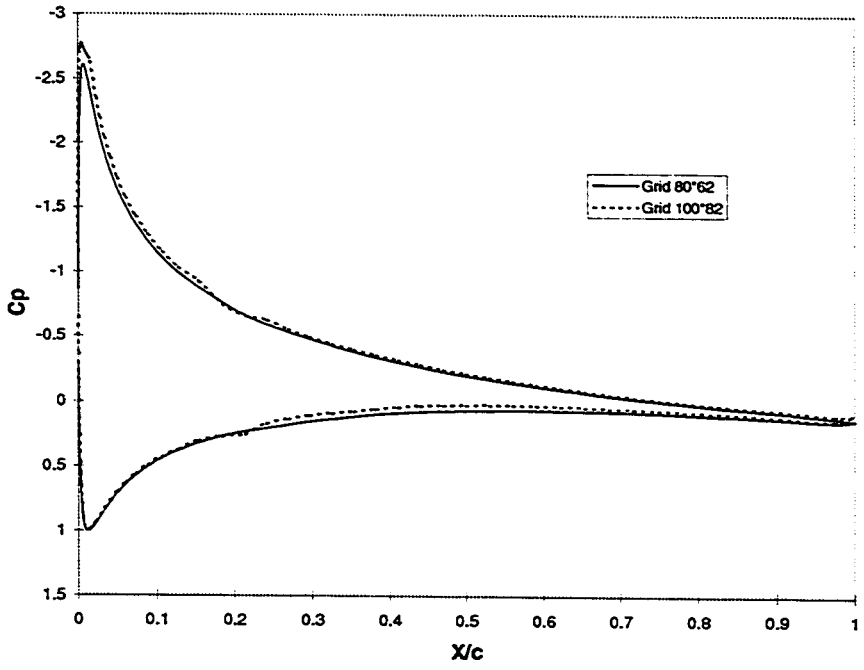

Figure 5.9: Surface Mean Pressure Coefficients for the infinite cascade for two different grid arrangements at $\alpha = 20^0$, Stagger=30^0 and C/S=0.83

(a)

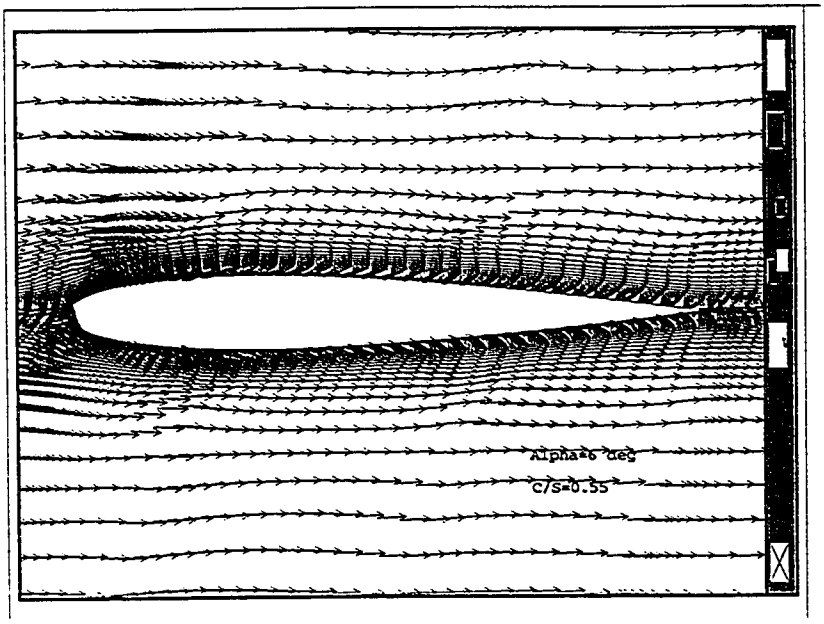

(b)

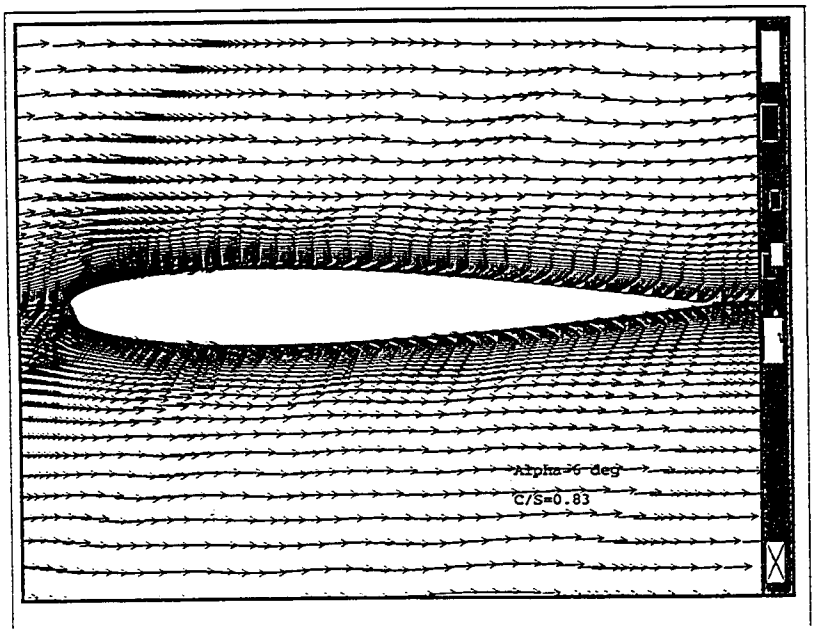

Figure 5.10: Velocity vector fields for the infinite cascade at $\alpha = 6^0$ and Stagger=30^0, for solidity ratios of (a) C/S=0.55 (b) C/S=0.83

(a)

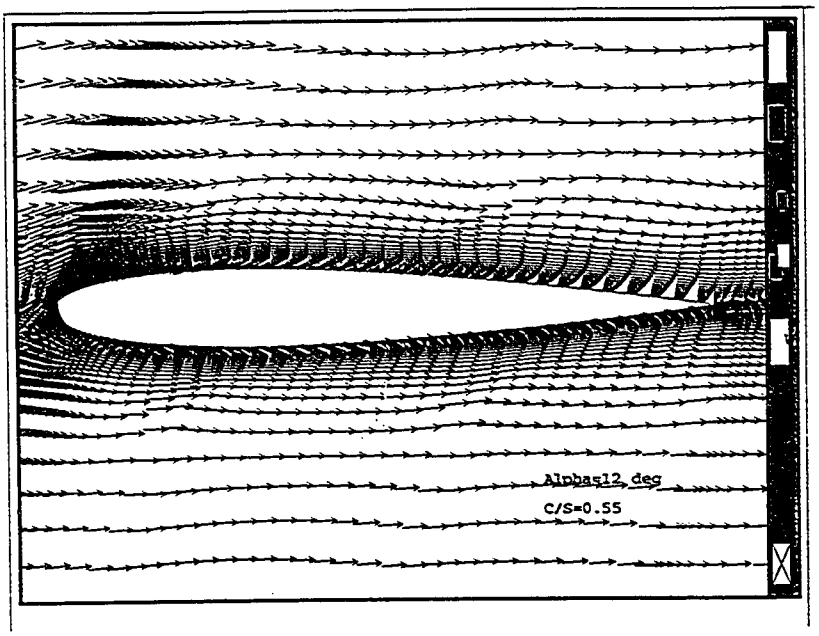

(b)

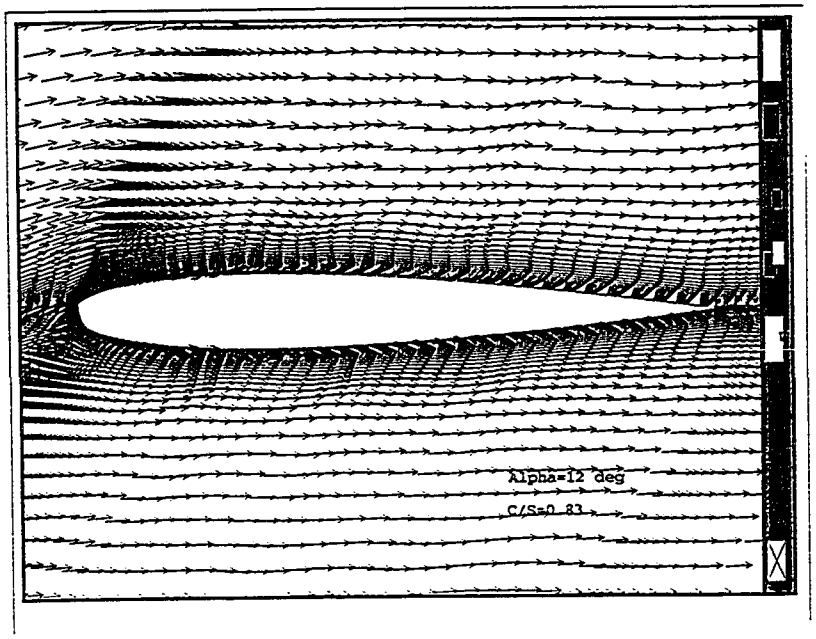

Figure 5.11: Velocity vector fields for the infinite cascade at $\alpha = 12^0$ and Stagger=30^0, for solidity ratios of (a) C/S=0.55 (b) C/S=0.83

(a)

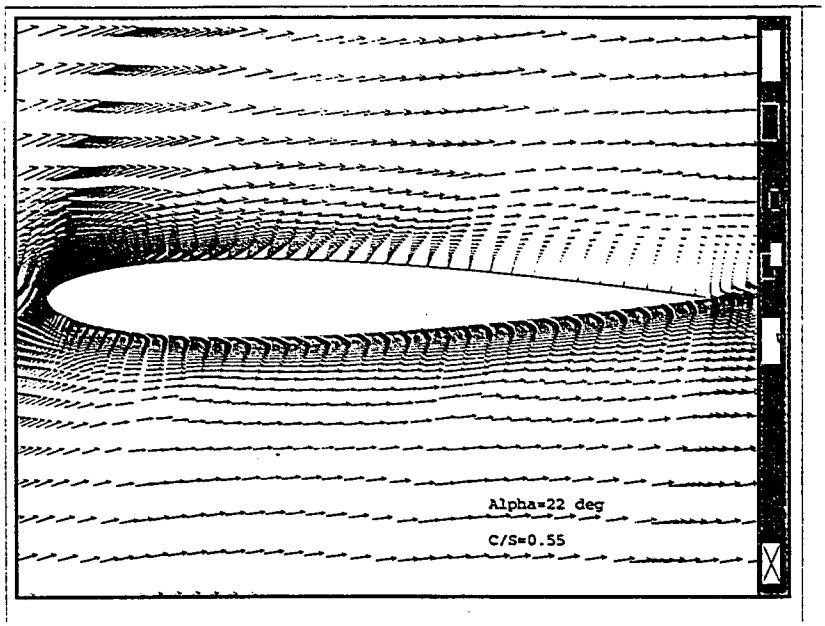

(b)

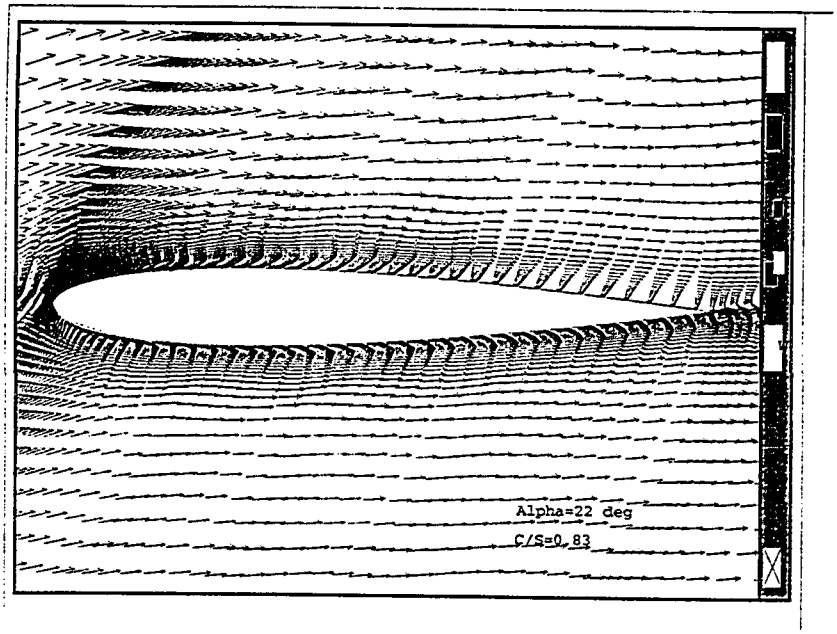

Figure 5.12: Velocity vector fields for the infinite cascade at $\alpha = 22^0$ and Stagger=30^0, for solidity ratios of (a) C/S=0.55 (b) C/S=0.83

(a)

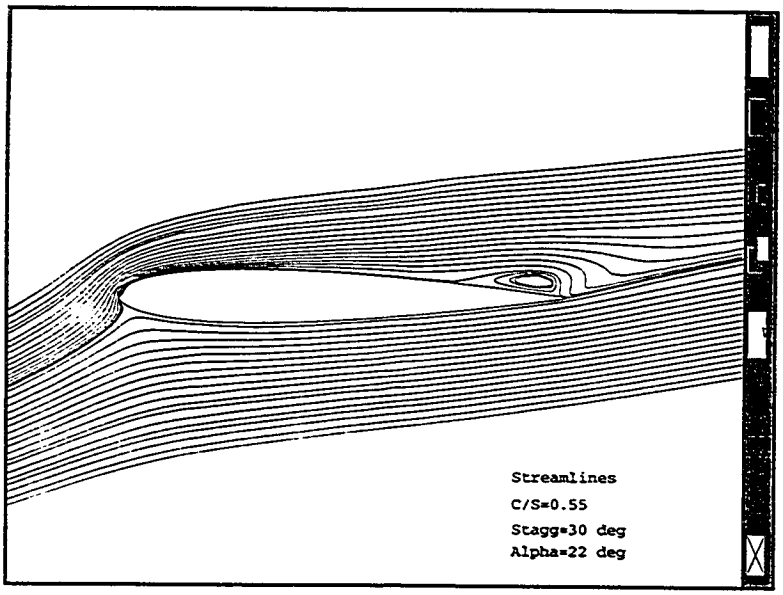

(b)

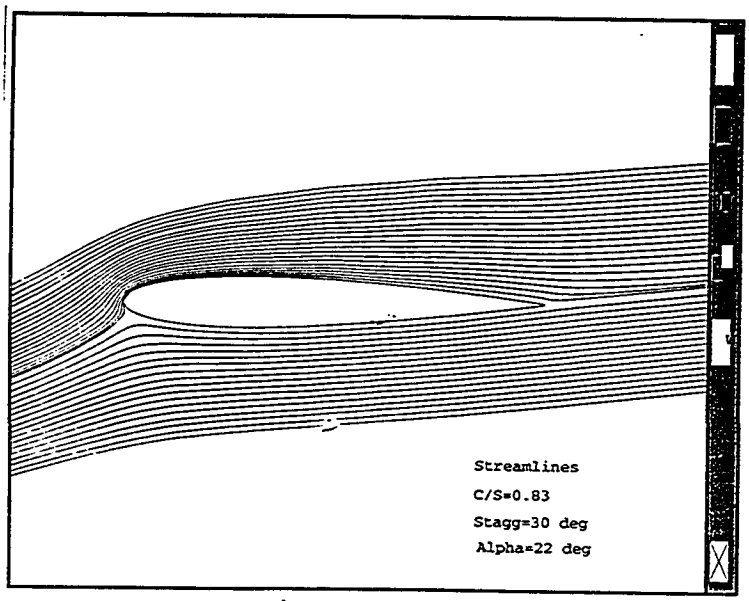

Figure 5.13: Streamline contours for the infinite cascade at $\alpha = 22^0$, Stagger=30^0, for solidity ratios of (a) C/S=0.55 (b) C/S=0.83

(a)

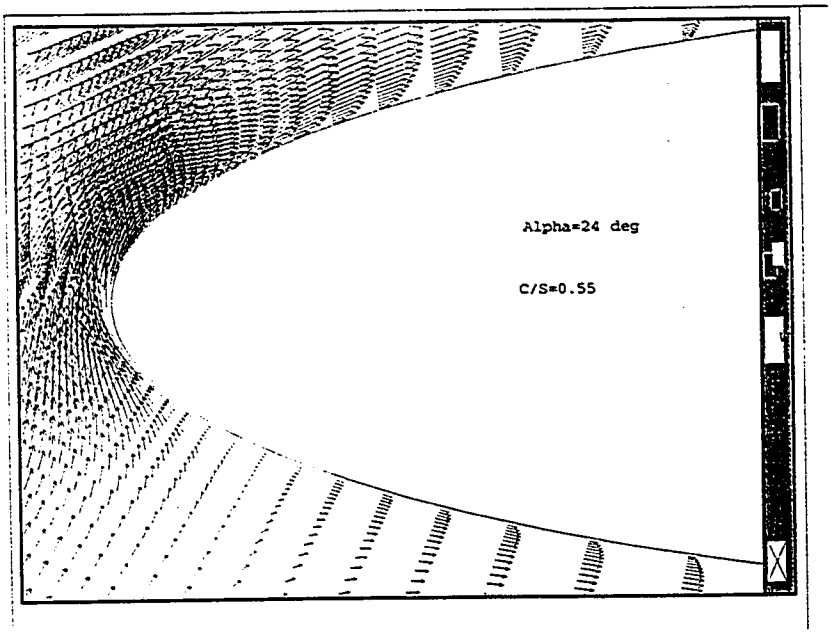

(b)

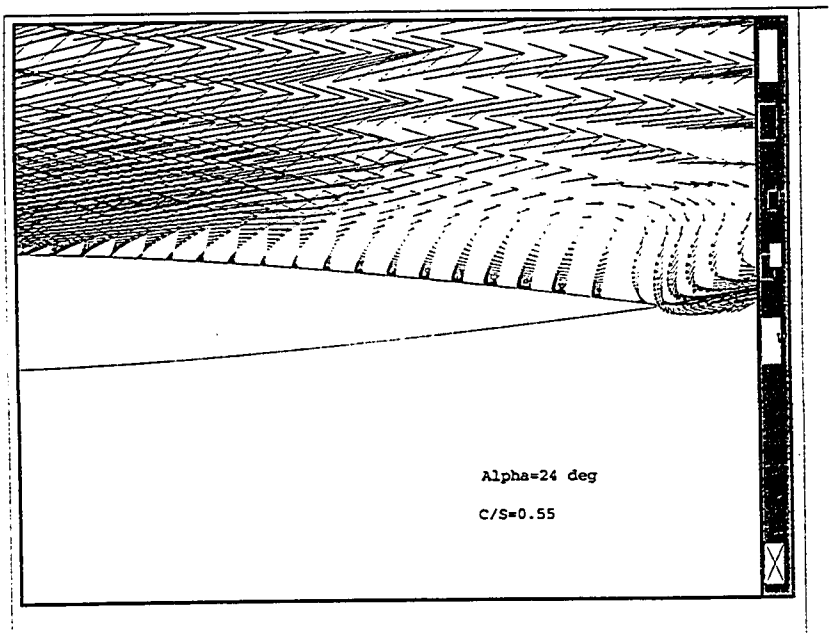

Figure 5.14: Enlarged views of the velocity vector fields for the infinite cascade C/S=0.55, $\alpha = 24^0$, Stagger=30^0

(a)

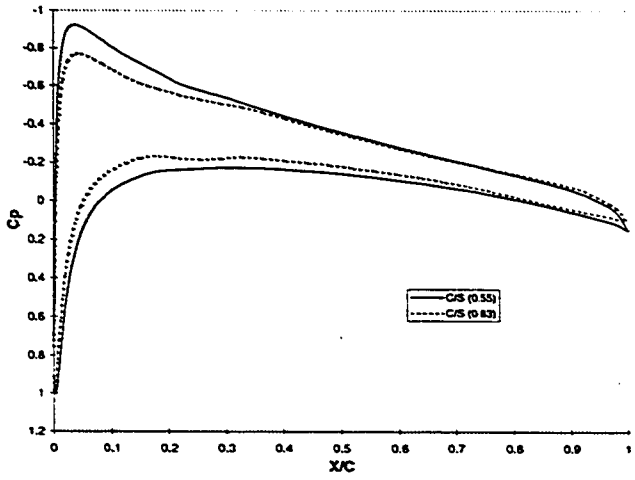

(b)

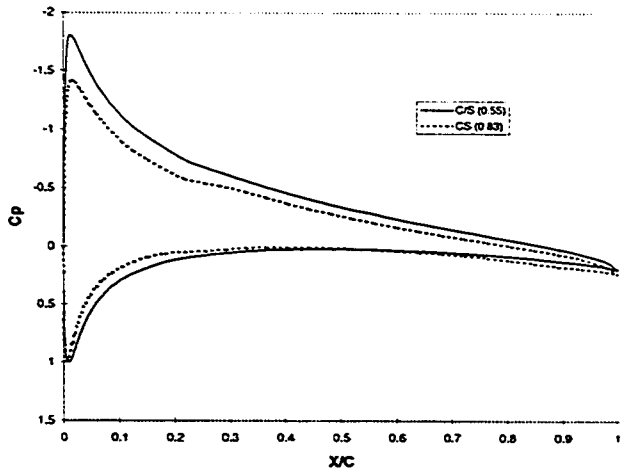

(c)

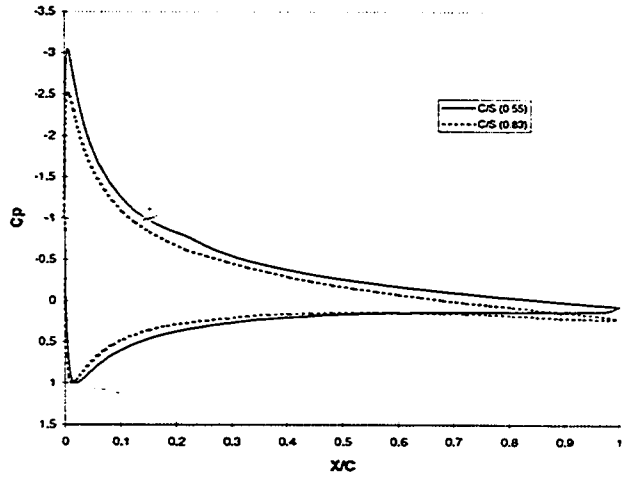

Figure 5.15: Effect of cascade solidity ratio on the surface mean pressure coefficients at different angles of attack (a) 6^0 (b) 12^0 (c) 20^0

(a)

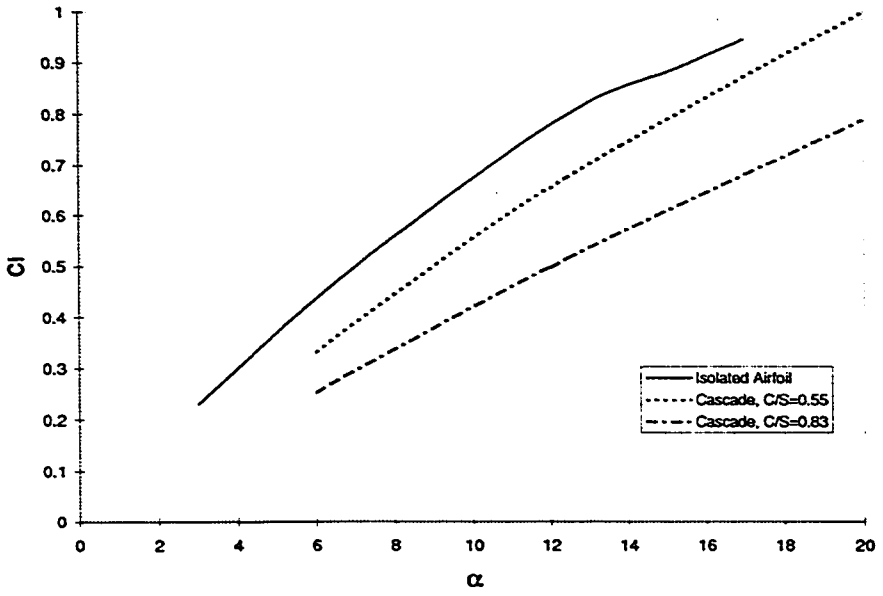

(b)

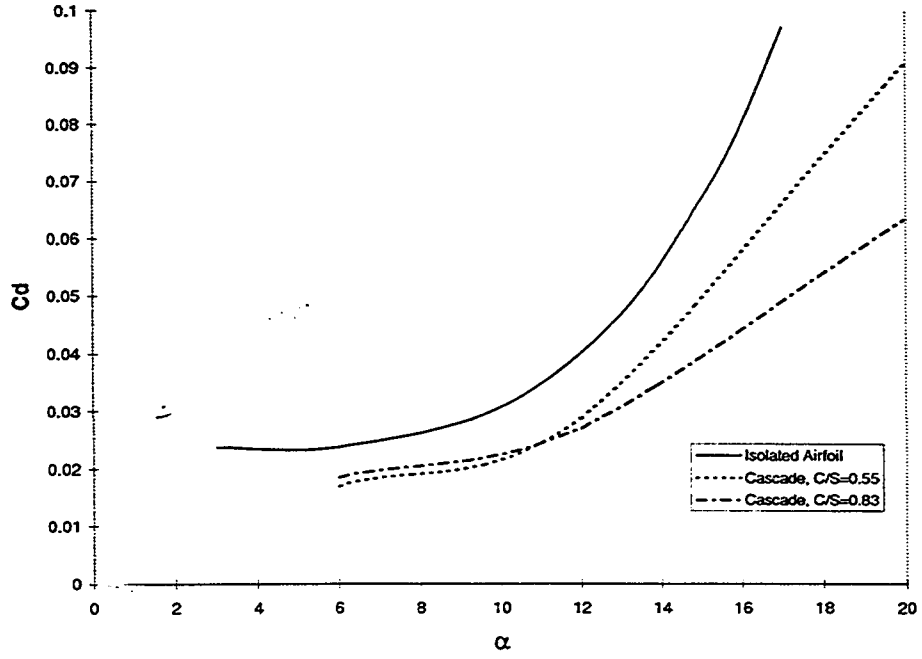

Figure 5.16: Effect of cascade solidity ratio on (a) Lift Coefficient (b) Drag Coefficient

Figure (5.21) shows the pressure coefficients corresponding to the two cases of stagger angles at different angles of attack. For all the cases, the pressure coefficient has a large suction peak at the suction surface near the leading edge. This is followed by a gradual increase in pressure. The lower surface has the stagnation point near the leading edge, where the pressure attains its maximum value. This is then followed by a favorable pressure gradient along the chord. At high angles of attack, the airfoils with a lower stagger attain a larger value of suction peak. This is due to a large flow spilling as being observed in the velocity field for the two cases. These curves show that at the trailing edge, the difference between pressures on the upper and lower surfaces is larger for airfoils with higher stagger (30^0). Consequently, the contribution of trailing edge pressure distribution in generating the lift is significant at higher staggers. At 6^0 angle of attack, the trailing edge pressure distribution is even more responsible for producing the lift. It should be be noted that the pressure distribution at lower surfaces of the airfoils is almost similar for either value of stagger.

Figure (5.22) shows the variation of lift and drag coefficients with the angle of attack. For both cases, the lift increases with an increase in incidence. The trend is almost the same as we observed for the case of solidity effects. The 30^0 staggered airfoils show a small value of drag. One of the reasons for this is that they have a lower flow spilling and hence the velocity gradient is not that sharp as compared to

(a)

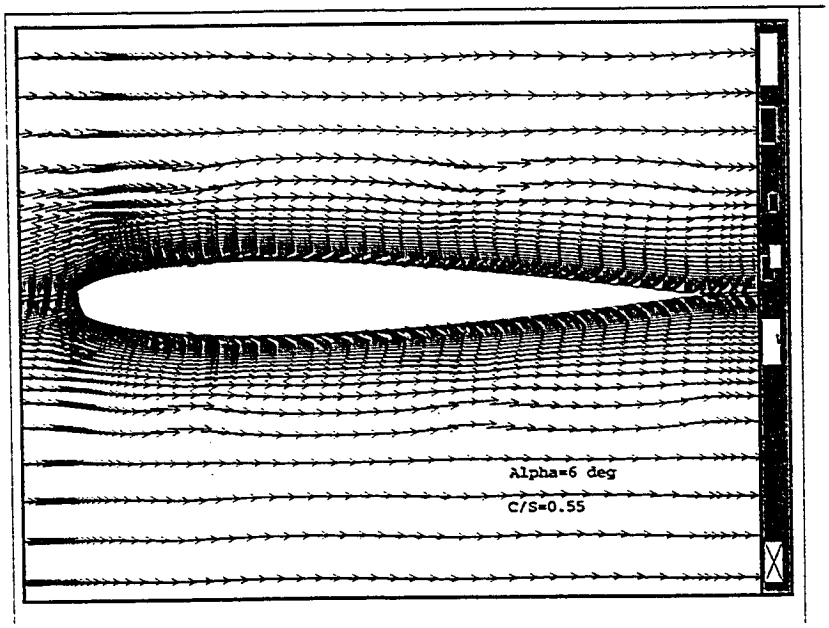

(b)

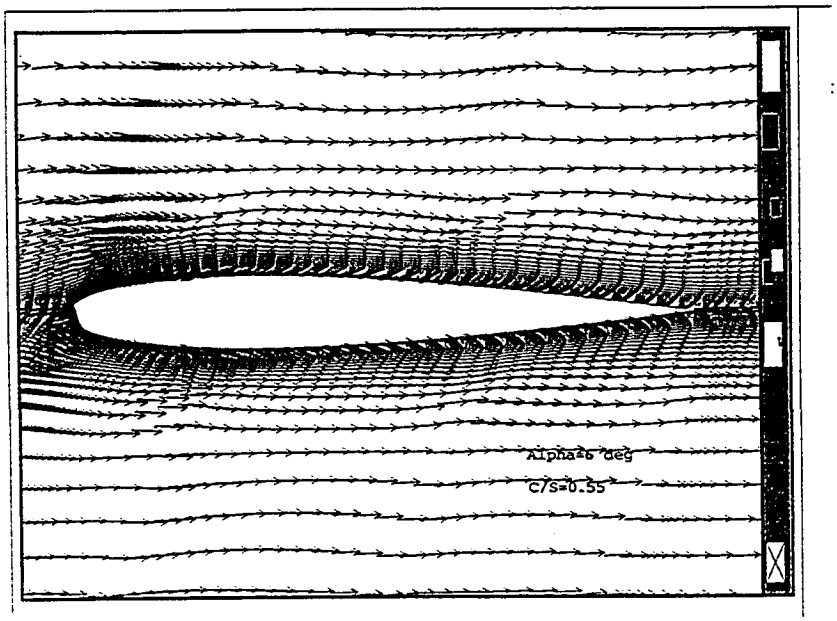

Figure 5.17: Velocity vector fields for the infinite cascade at $\alpha = 6^0$, C/S=0.55, for (a) Stagger=10^0 (b) Stagger=30^0

(a)

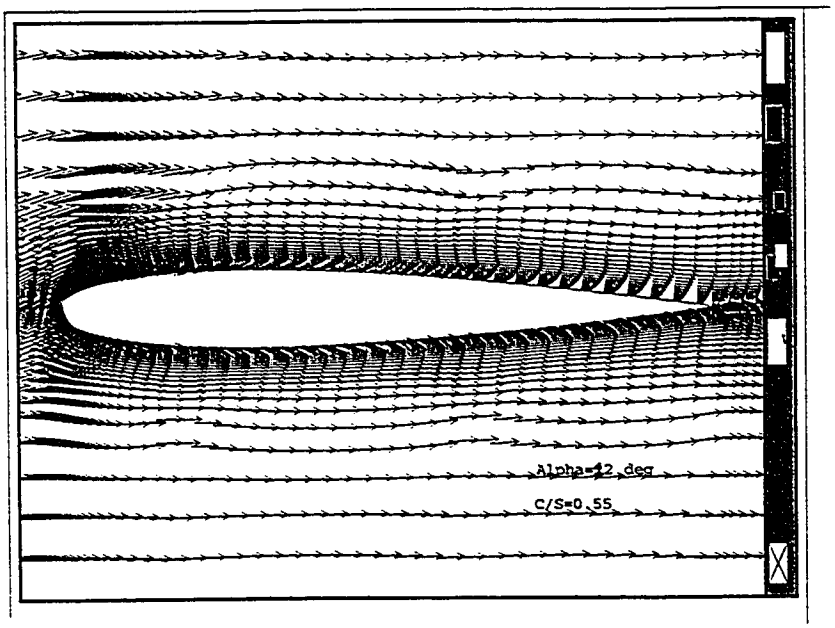

(b)

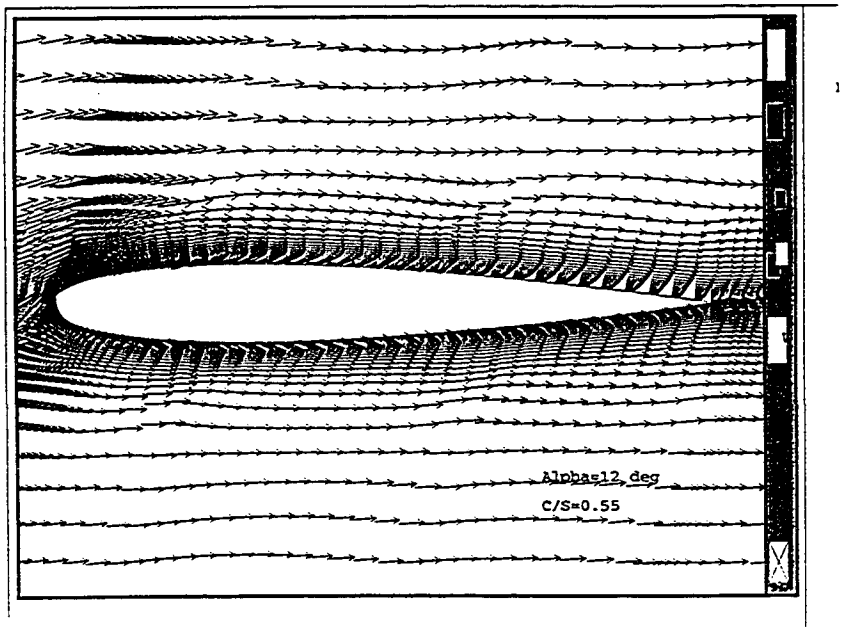

Figure 5.18: Velocity vector fields for the infinite cascade at $\alpha = 12^0$, C/S=0.55, for (a) Stagger=10^0 (b) Stagger=30^0

(a)

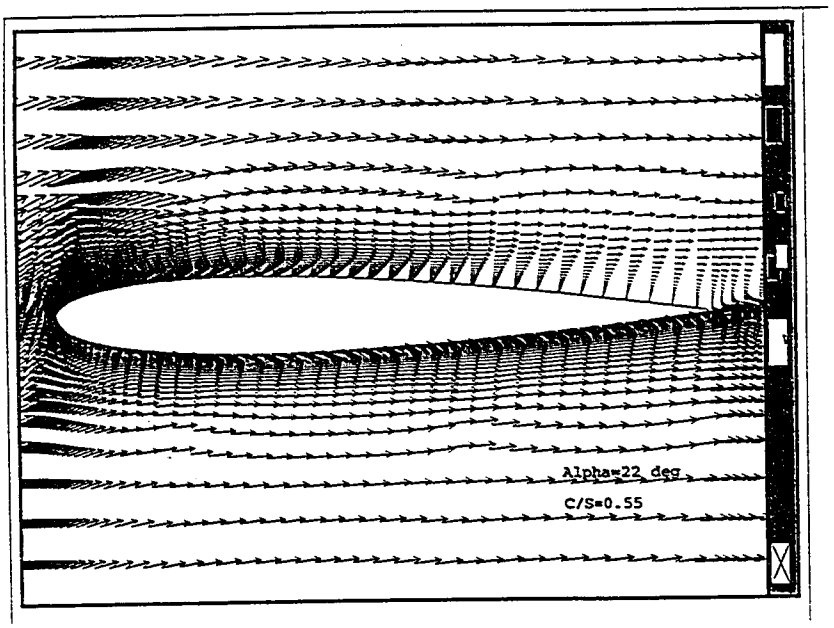

(b)

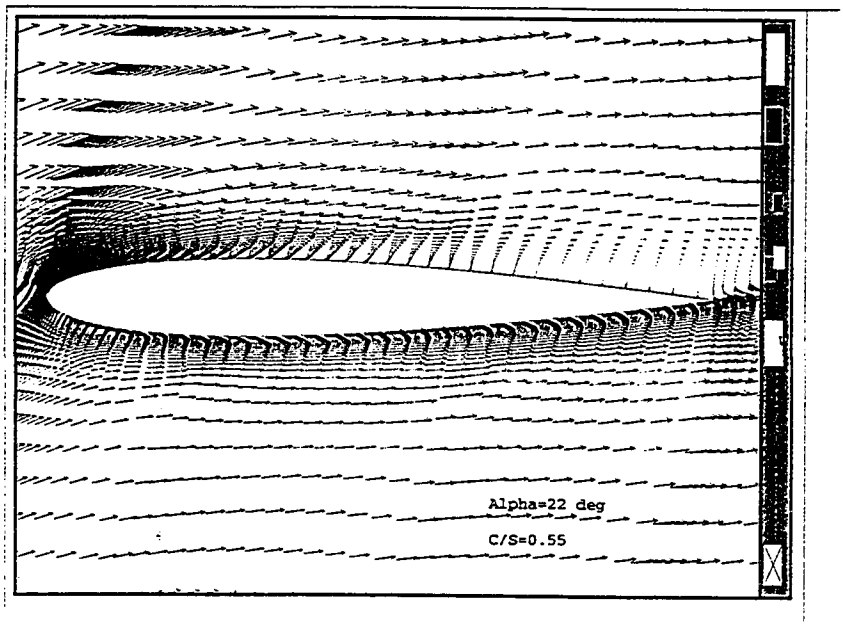

Figure 5.19: Velocity vector fields for the infinite cascade at $\alpha = 22^0$, C/S=0.55, for (a) Stagger=10^0 (b) Stagger=30^0

(a)

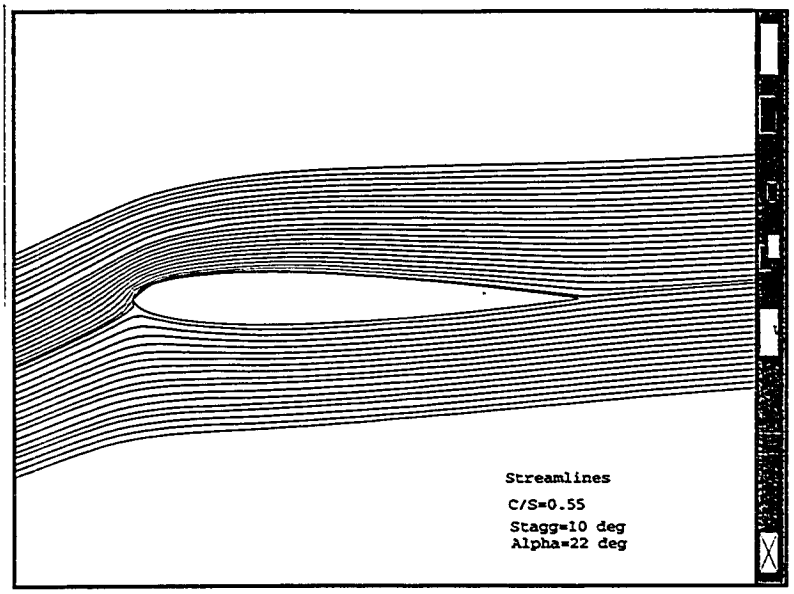

(b)

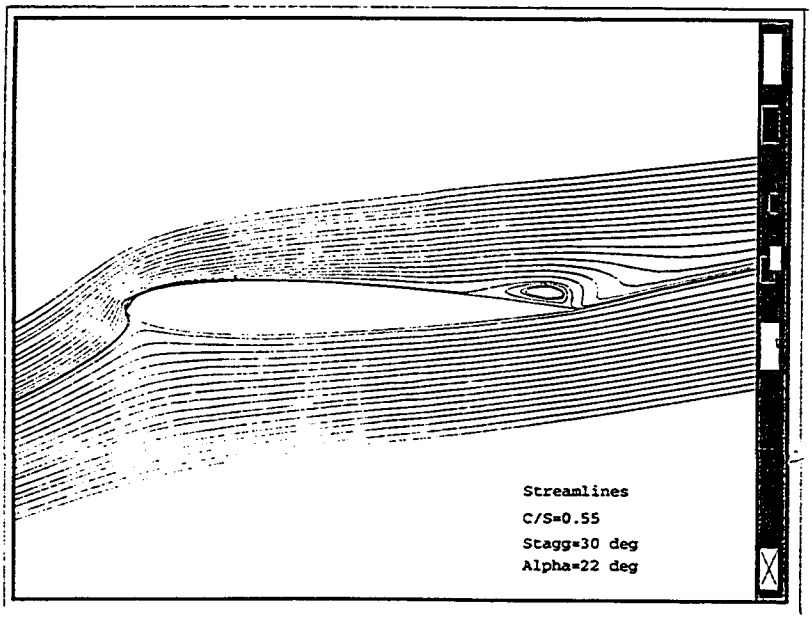

Figure 5.20: Streamline contours for the infinite cascade at $\alpha = 22^0$, C/S=0.55, for (a) Stagger=10^0 (b) Stagger=30^0

10^0 staggered airfoils, so, they posses a lower skin friction.

5.4 Effect of rotation of the airfoil nose

From the previous discussions it is evident that the lift is mostly generated at the leading edge of the airfoil. The lower surface of the airfoil has a high pressure region, because of the occurrence of the stagnation of the incoming flow at the leading edge. This causes a spilling of the incoming flow towards the upper surface. Consequently very high velocity gradients develop on the upper surface accompanied by very small pressures which is called as suction peak. This difference in pressures at the two surfaces of the airfoil generates a lift. If we could, some way, further increase the velocity on the upper surface and reduce the velocity at the lower surface, then pressure differential between both surfaces of the airfoil will increase. This will result in an increase in the lift.

The above described task could be accomplished by moving the suction surface of the airfoil in the direction of flow and the pressure surface of the airfoil in the direction opposite to the flow. This will result in a large increase in the lift and a large decrease in the drag, since the separation which appears at large incidences will vanish. However it is very difficult to implement this idea in real systems. A

relatively easier task is to rotate only the nose of the airfoil since it has a circular curvature and can be considered a separate piece from the rest of the airfoil.

In the present study this case has been tested to explore the potential advantages, if they are significant. The isolated airfoil at three different angles of attack ($13^0, 15^0, 16^0$) has been analysed. Five percent of the chord on each of the suction and pressure surfaces of the airfoil has been specified with a wall velocity such that at the upper surface, this velocity is in the direction of flow whereas at the lower surface it is in the direction opposite to that of the flow. The free stream velocity of the incoming flow is set at 50 m/s. Two values of tangential velocities as 50m/s and 150 m/s, have been considered for the leading edge rotation velocity.

Figure (5.23) shows the pressure coefficients for the two rotational cases at different angles of attack. We find that upto the extent of 25% chord length there is an increase in the pressure difference between the upper and the lower surfaces. Afterwards, although in comparison to the case without rotation, the pressure on both the upper and lower surfaces has increased somewhat, but the difference in pressure is almost identical for the two cases (i.e. with and without rotation). It is observed that the effect of leading edge rotation is more pronounced for a higher angle of attack (16^0) as compared to a lower angle of attack. It is quite apparent that a high rotational velocity causes high pressure difference to occur between the

two surfaces. Hence, a rotating velocity of 150m/s is found to be more promising for increasing the lift.

In the light of the above discussions, another case has been considered in which rotational velocity has been set at 150m/s whereas the 11% chord length has been specified with a wall velocity. Figure (5.24) shows the velocity vector for this case and for the case of no leading edge rotation, at an angle of attack of 16^0. Figure(5.25) shows the streamline plots for the same cases. We observe that there is an increased flow spilling at the leading edge. The separation point has shifted downward towards the trailing edge and a reduction in the wake size is quite evident in the streamline plot. However, we find that there is no significant effect on the separation region and still large separation occurs at the leading edge, therefore, the effect of leading edge surface rotation seems to be very localized. If the separation could be delayed to a significant extent then this method could be very advantageous.

Figure (5.26) shows the pressure coefficients for the two cases at different angles of attack. We observe that suction peak has increased in magnitude for 11% leading edge chord rotation. This has a positive effect on the lift generated. At the trailing edge, the pressure difference is essentially the same. On the pressure surface we observe a pressure kink. This is due to the fact that airfoil surface has a velocity upstream of this point whereas it has zero velocity downstream of this point.

Figure (5.27) shows the lift and drag coefficients for the two cases. The case of rotating nose has been simulated for only three different angles of attack since at lower angle of attack there is no separation, so, there is no effect of delaying of separation by this practice. It is observed that there is an increase in the lift in the case of the rotating nose as compared to the non-rotating nose airfoil. It is further observed that lift increases with the increase in the the percentage of the length of the chord that rotates. The slope of the curve for the flow field around non-rotating nose airfoil declines earlier but the lift curve corresponding to the rotating nose airfoil retains the same slope as being there at lower incidences.

Decrease in drag occurs and the reduction in drag increases with the increasing angle of attack. The reduction in drag is more pronounced for 11% x/c surface rotation at leading edge. At 16^0 the reduction in drag is quite significant. The slope of the drag curve reduces.

As the present object is to find ways to increase the lift and reduce the drag, therefore, the conclusions derived indicates that increase in the rotational velocity and the extent of rotating chord length, both have positive effect on increasing the lift and reducing the drag. However, we have not seen quite significant effects as the separation region has only reduced in size, but not totally eliminated. In the last simulation the whole airfoil surface is set to rotate with some velocity.

Figure (5.28) shows the flow field at 16^0 angle of attack for full rotation of the airfoil surface. It is evident that the situation has turned to be quite dramatic. The separation has totally disappeared and a high flow spilling is observed at the upper surface.

Figure (5.29) shows the corresponding pressure curve and it can be seen that a tremendous increase in the pressure difference between the upper and the lower surfaces of the airfoil occurs. The disappearance of separation has brought about a large decrease in the pressure on the upper surface. This produces a large increase in the lift.

(a)

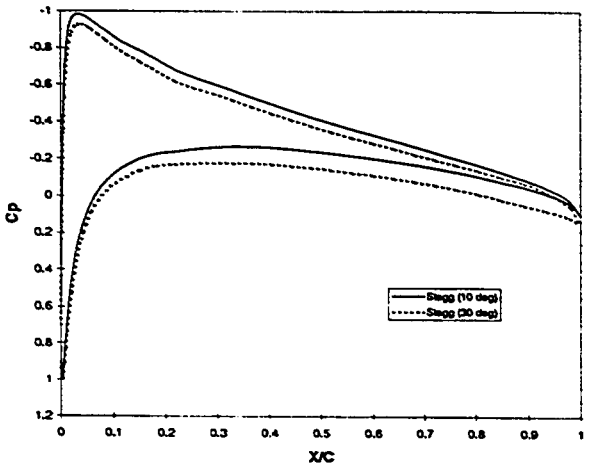

(b)

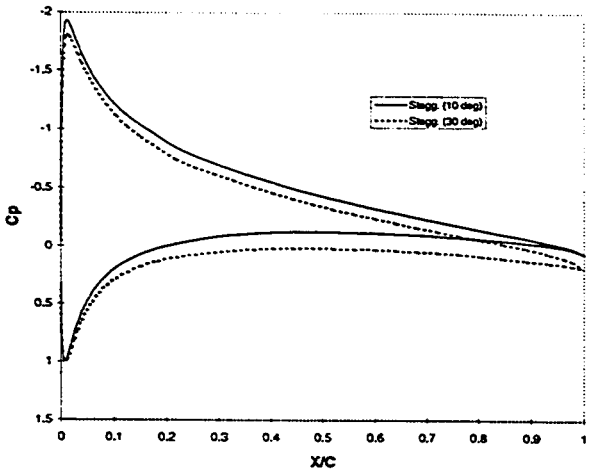

(c)

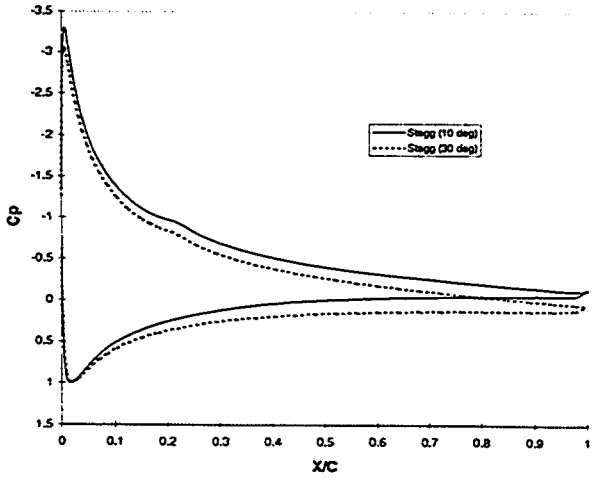

Figure 5.21: Effect of cascade stagger angle on mean pressure coefficients at different angles of attack (a) 6^0 (b) 12^0 (c) 20^0

(a)

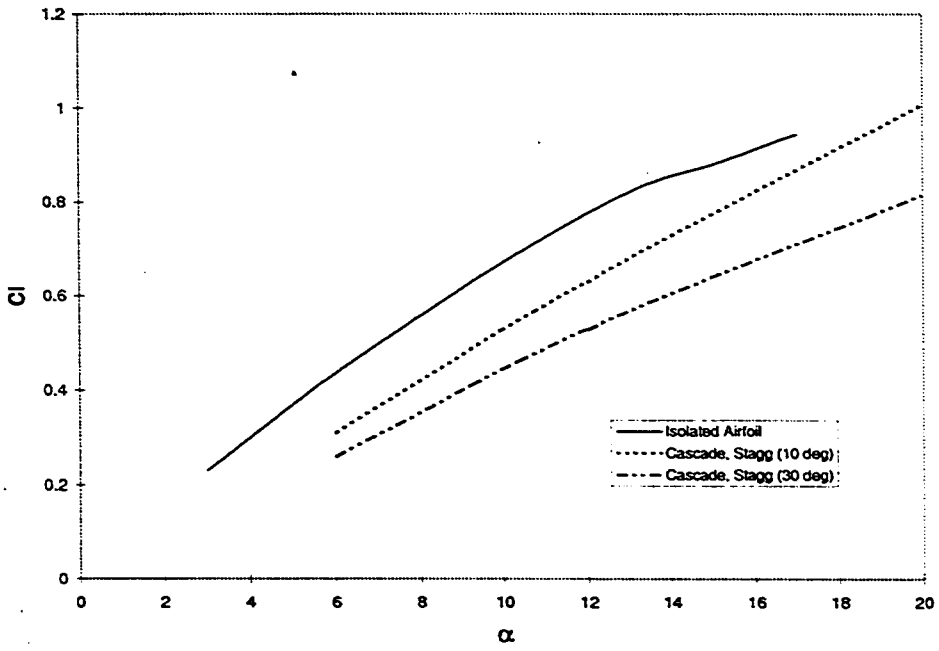

(b)

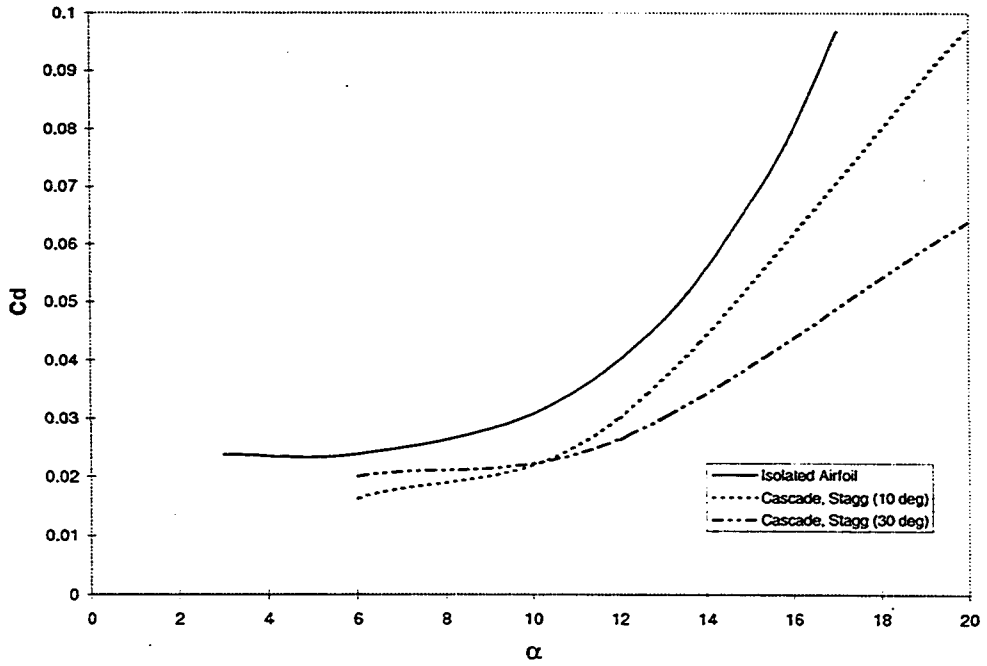

Figure 5.22: Effect of cascade stagger angle on (a) Lift Coefficient (b) Drag Coefficient

(a)

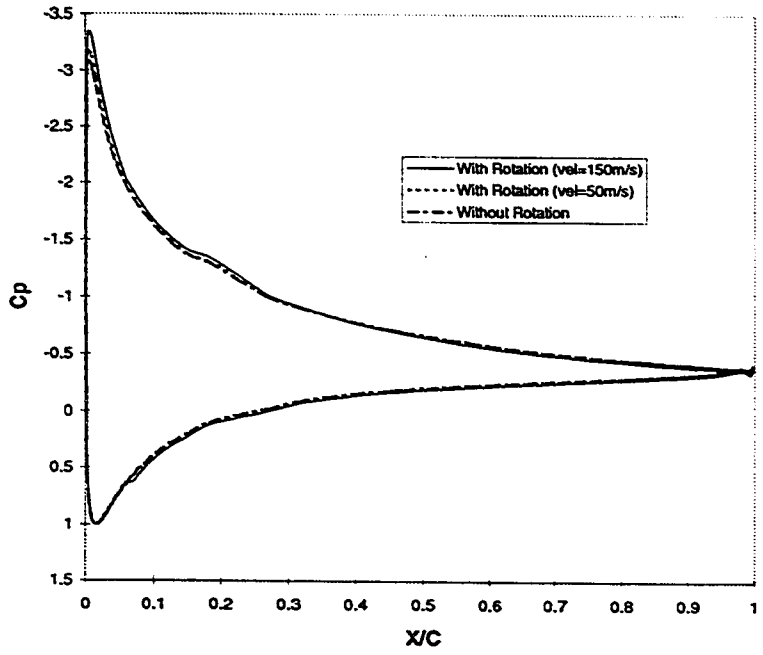

(b)

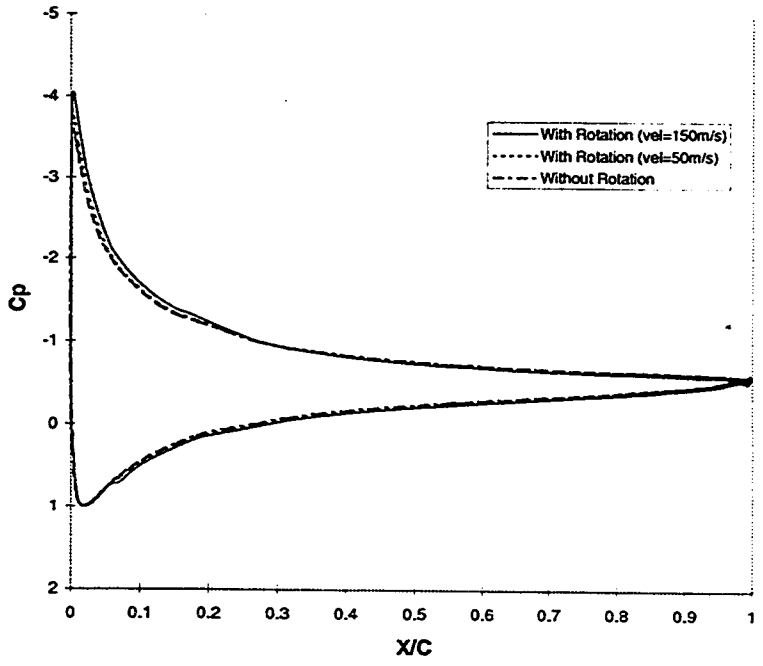

Figure 5.23: Effect of leading edge rotational velocity on mean pressure coefficient at different angles of attack (a) 13^0 (b) 16^0

(a)

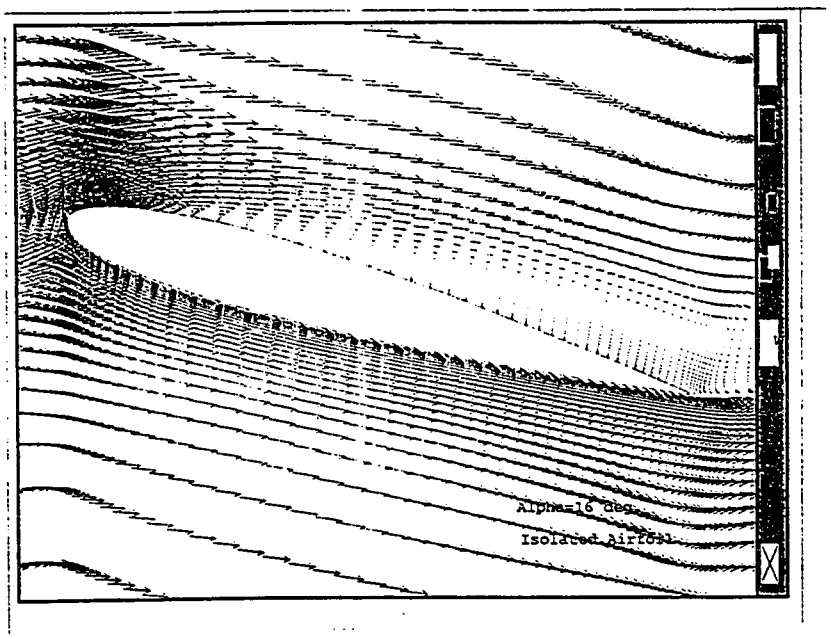

(b)

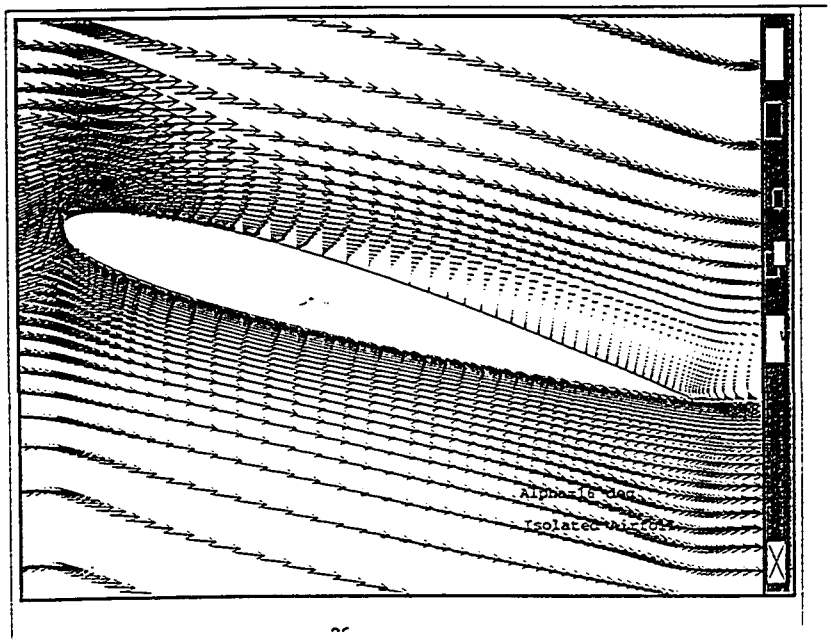

Figure 5.24: Velocity vector fields for the Isolated Airfoil (a) Without (b) With leading edge rotation at $\alpha = 16^0$

(a)

(b)

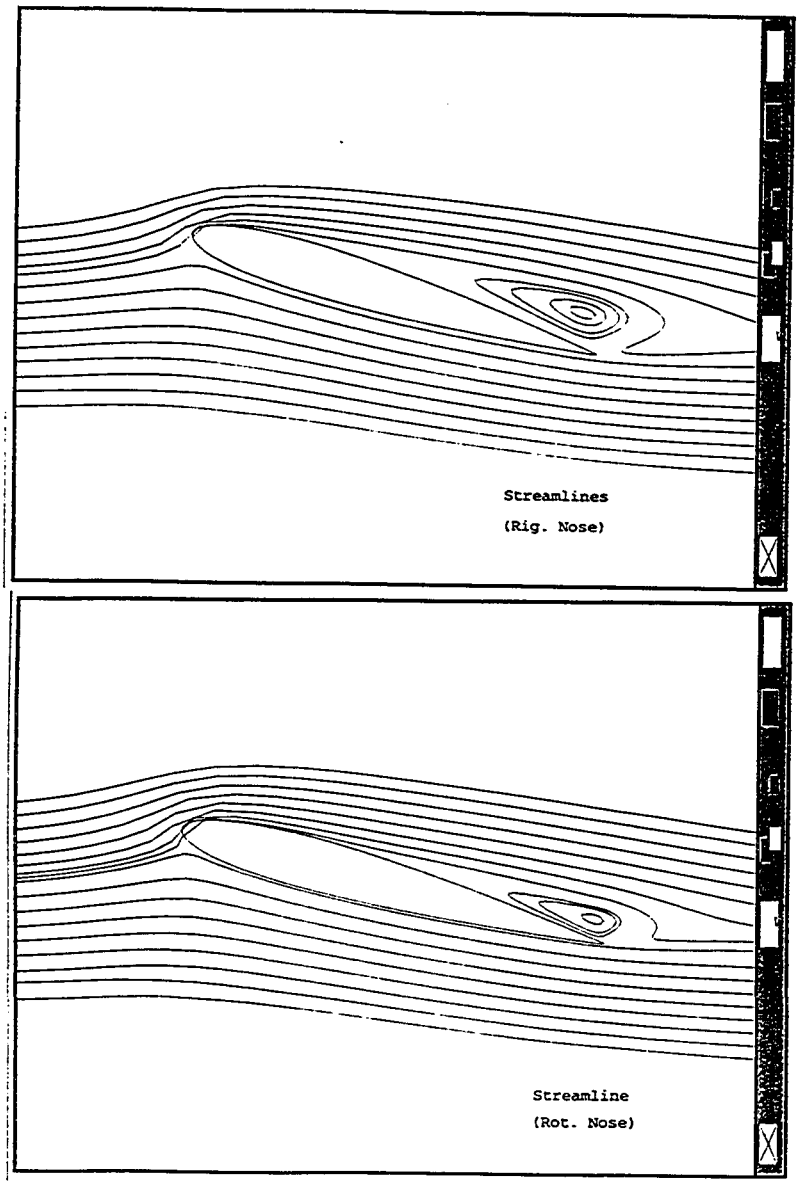

Figure 5.25: Streamline contours for the Isolated Airfoil (a) Without (b) With leading edge rotation at $\alpha = 16^0$

(a)

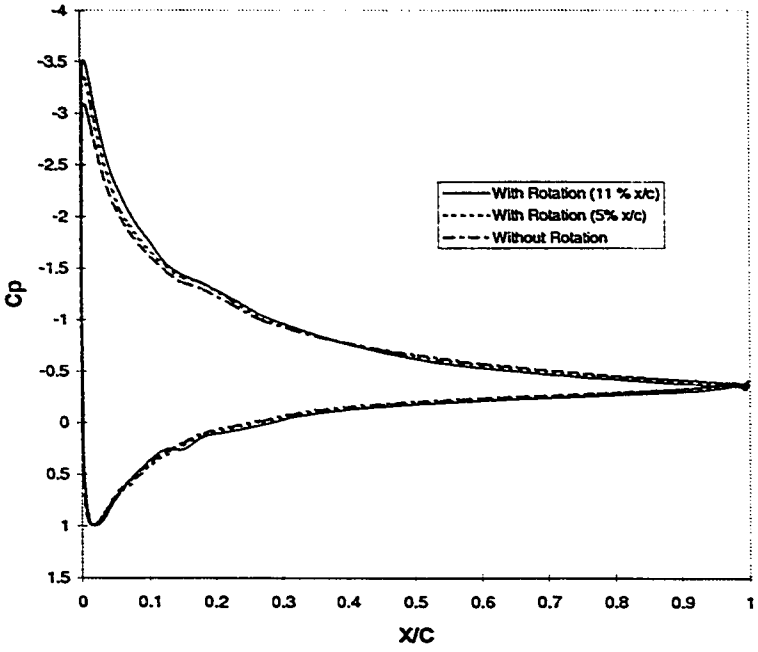

(b)

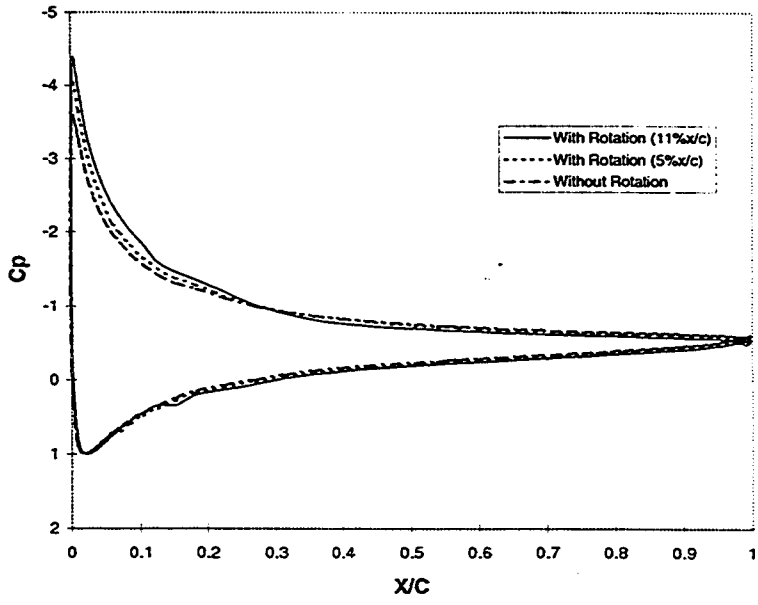

Figure 5.26: Effect of increase in rotating chord length on mean pressure coefficient at different angles of attack (a) 13^0 (b) 16^0

(a)

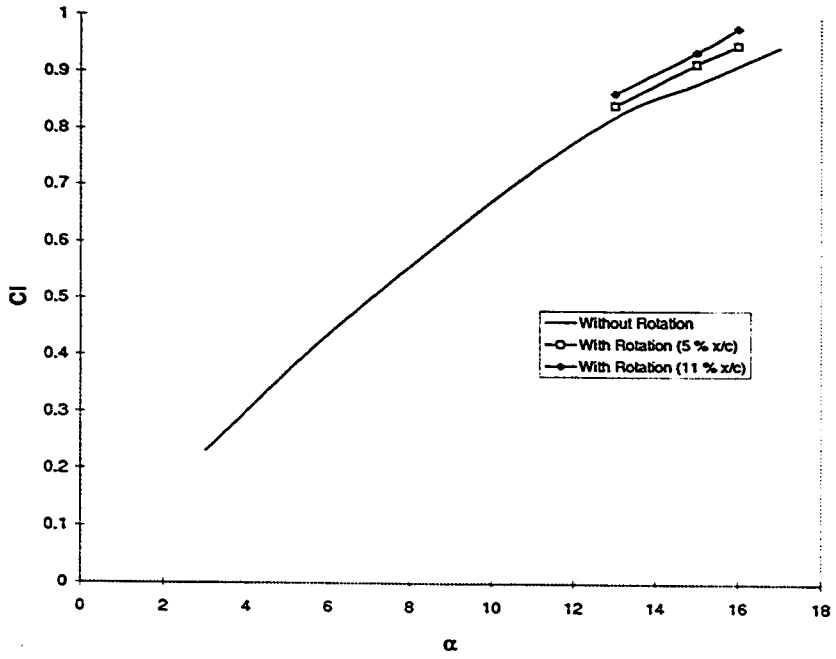

(b)

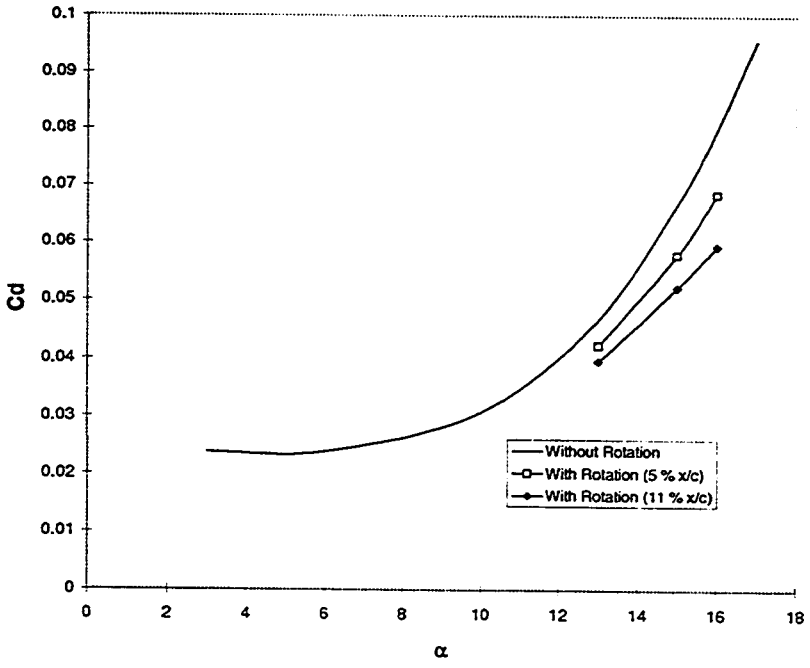

Figure 5.27: (a) Lift Coefficients (b) Drag Coefficients for the isolated airfoil with and without leading edge rotation

(a)

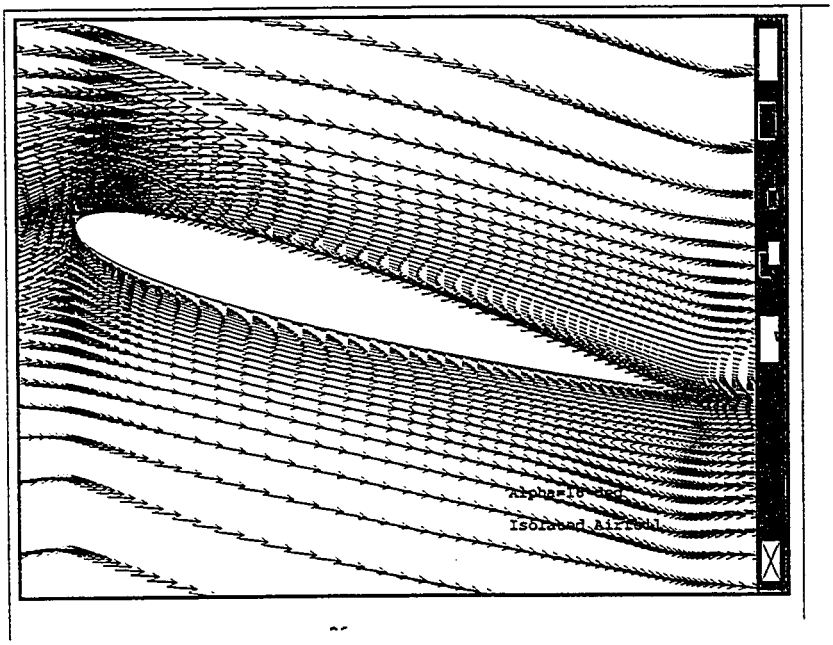

(b)

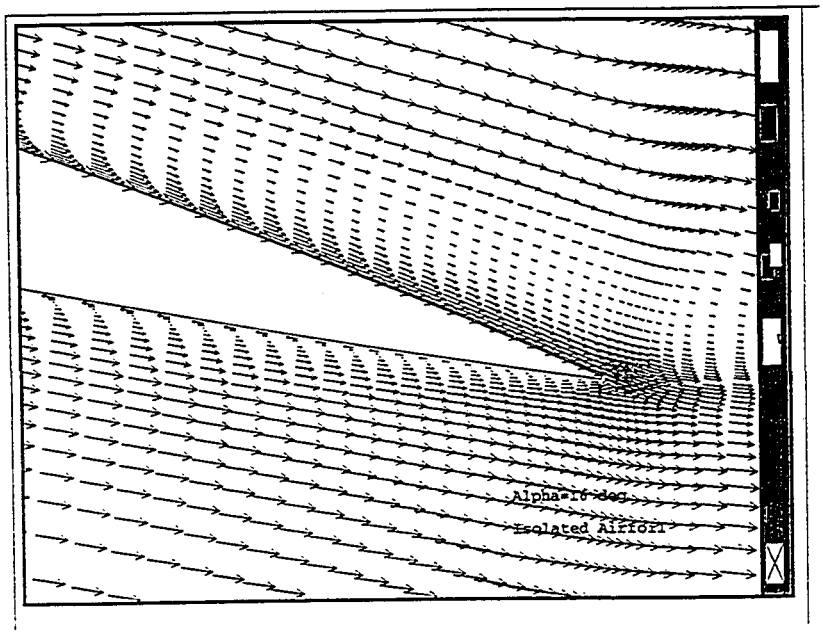

Figure 5.28: (a)Velocity vector fields for the isolated airfoil at 16^0 angle of attack for the whole surface rotation (b) Enlarged view of the effect of rotation

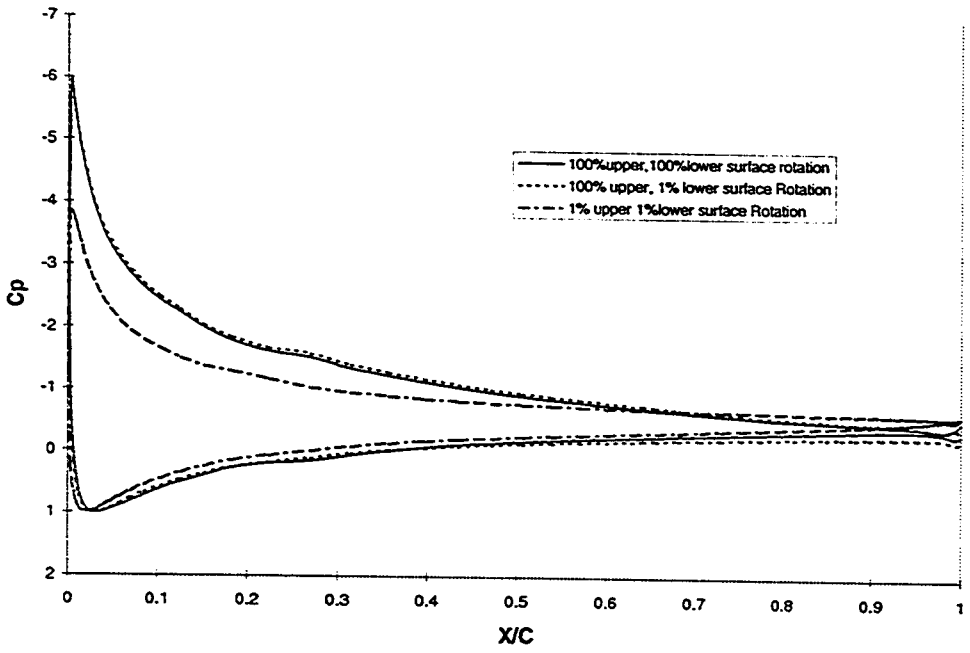

Figure 5.29: Pressure Coefficients obtained after full surface rotation for the isolated airfoil

Chapter 6

CONCLUSIONS

PHOENICS code has been used to simulate the flow field around the isolated single and cascade of NACA 0012 airfoils. Attached and separated flows have been computed using the k-ϵ turbulence model. Lift, Drag and Pressure coefficients have been determined.

The conclusions derived for the flow field investigated are as follow.

- High degree of flow spilling occurs at the leading edge of the airfoil for high angle of attack. This, then, results in separation at the trailing edge. The point of separation moves towards the leading edge when solidity (c/s) increases . The effect of pressure suppression is quite evident.

- With the increase in incidence the adverse pressure gradient attains large values.

- The boundary layer thickness increases towards the trailing edge as the angle of attack increases. The rate of this increase reduces at low solidity.

The conclusion obtained from the pressure, lift and drag coefficients may be listed as follows.

- Pressure coefficient on the suction surface at the trailing edge attains high values with incidence and with a decrease in the solidity.

- Slope of Lift coefficient curve vs angle of attack reduces as large separation occurs. However, this has not been predicted to be drastic as being observed in experiments. Further, the incidence angle at which a drop in the lift will occur has a larger value as compared to the experimental data available . This may be due to the steady state analysis employed in the computation. In this case, once the separation occurs, the vortex developed stays as it forms rather than detaching from the surface and forming the vortex shed. Therefore the lift coefficient predicted immediately after the separation may not agree well with the experimental results.

- As the solidity increases the incidence at which maximum lift is obtained, increases.

- At high incidences, an increase in lift is obtained by decreasing the stagger angle of airfoils in the cascade. A slight increase in drag is also observed.

- The angle of attack at which separation appears, also, increases. As a result, the maximum obtainable lift is larger for the cascade corresponding to a lower stagger angle.

The conclusion obtained for rotating the nose of the airfoil is as follow.

- With only nose rotation of the airfoil, the increase in lift and decrease in drag has not been found to be very significant. This may be due to the fact that present study is unable to predict a drastic decrease in the lift and increase in the drag at stall point. For real airfoil systems the advantages may be significant. However, the lift coefficient increases drastically while drag coefficient reduces as the full surface of the airfoil is rotated, in this case, separation vanishes.

Bibliography

[1] A. T. Sayers, "Hydraulic and Compressible Flow Turbomachines," *McGraw Hill Book Company. England* 1990

[2] J. P. Gostelow, "Cascade Aerodynamics," *Pergammon Press England* 1984

[3] Ira H. Abbott and Albert E. Von Doenhoff, "Theory of Wing Sections Including a Summary of Airfoil Data,".*Dover Publications. Inc.. New York* Corrected Reprint of the First Edition (1949)

[4] Donald P. Rizzetta and Miguel R. Visbal, "Comparative numerical study of two turbulence models for airfoil static and dynamic stall," *AIAA Journal*, vol. 31, No. 4, April 1993, pp. 784-786

[5] Day I. J., "Stall inception in axial flow compressors," *Journal of turbomachinery*, Vol. 115, January 1993, pp. 1-9

[6] Ali Koc, Yilbas B. S. and Baltacioglu E., "Some observations on stall behavior of an isolated compressor rotor," *Mechanical Incorporated Engineer*, February

1992, pp. 7-14

[7] Lars Davidson and Arthur Rizzi, "Navier Stokes stall predictions using an algebraic Reynolds-stress model," *Journal of spacecraft and rockets*, vol. 29, No. 6, Nov.- December 1991, pp. 794-800

[8] Jon A. Hoffmann. "Effects of free stream turbulence on the performance characteristics of an airfoil," *AIAA Journal*, vol. 29, No. 9, September 1991, pp. 1353-1354

[9] D. W. Zingg and G. W. Johnston, "Interactive airfoil calculations with higher-order viscous-flow equations," *AIAA Journal*, vol. 29, No. 7, July 1991, pp. 1033-1040

[10] G.A. Osswald, K.N. Ghia and U. Ghia, "Simulation of dynamic stall phenomenon using unsteady Navier-Stokes equations," *Computer Physics Communication*, vol. 65, No. 1-3, 1991, pp. 209-218

[11] Davoudzadeh F., Liu N. S., Shamroth S. J. and Thoren S. J., "Navier Stokes study of rotating stall in compressor cascades," *AIAA Journal*, vol. 28, March 1990, pp. 492-498

[12] Jonnavithula, Thangam S. and Sisto F., "Computational and experimental study of stall propagation in axial compressors," *AIAA Journal*, November 1990, pp.1945-52

[13] Mitcheltree R. A., Salas M. D. and Hassan H. A., "One equation turbulence model for transonic airfoil flows," *AIAA Journal*, vol. 28, No. 9, September 1990, pp. 1625-1632

[14] Osama A Kandil and H. Andrew Chuang, "Unsteady transonic airfoil computation using implicit Euler scheme on body-fixed grid," *AIAA Journal*, vol. 27, No. 8, August 1989, pp. 1031-1037

[15] Mathioudakis K. and Breugelmans F. A. E., "Three dimensional flow in deep rotating stall cells of an axial flow compressor," *Journal of propulsion and power*, vol. 4, 1988, pp. 263-69

[16] J. Basuki and J. M. Graham, "Discrete vortex computation of separated airfoil flow," *AIAA Journal*, vol. 25, No. 11, November 1987, pp. 1409-1410

[17] Nakahashi Kazuhiro and Deiwert George S., "Self adaptive grid method with application to airfoil flow," *AIAA Journal*, vol. 25, No. 4, April 1987, pp. 513-520

[18] Yoshifumi Shida, Kunio Kuwahara, Kiyoaki Ono and Hideo Takami, "Computation of dynamic stall of a NACA 0012 airfoil," *AIAA Journal*, vol. 25, No. 3, March 1987, pp. 408-413

[19] C. G. Speziale, F. Sisto, S. Jonnavithula, "Vortex simulation of propagating stall in a linear cascade of airfoils," *Transactions of ASME-Fluids Engineering Division*, vol. 108, September 1986, pp. 304-312

[20] O. Schafer, H. H., Fruhauf, B. Bauer and M. Guggolz, "Application of a Navier-Stokes analysis to flows through plane cascades," *Journal of Engineering for Gas Turbines and Power*, vol. 108, January 1986, pp. 103-111

[21] Weinberg B. C., Yang R. J. and McDonald H., "Calculation of two and three dimensional transonic cascade flow fields using the Navier-Stokes equations," *Journal of Engineering for Gas Turbines and Power*, vol. 108, January 1986, pp. 93-102

[22] C. Hah, "Modelling of turbulent flow fields through a cascade of airfoils at stall conditions," *AIAA Journal*, vol. 23, No. 9, September 1985, pp. 1411-17

[23] Robert W. paterson and Harris D. Weingold, "Experimental investigation of a simulated compressor airfoil trailing-edge flow field," *AIAA Journal*, vol. 23, No. 5, May 1985, pp. 768-775

[24] Marsha J. Berger and Antony Jameson, "Automatic adaptive grid refinement for the Euler equations," *AIAA Journal*, vol. 23, No. 4, April 1985, pp. 561-568

[25] Bryanston Cross P. J. and Denton J. D., "Comparison of measured and predicted transonic flow around an airfoil," *AIAA Journal*, vol. 22, No. 8, August 1984, pp. 1025-26

[26] Das, D. K. and Jiang, H. K., "An experimental study of rotating stall in a multistage axial flow compressor," *Journal of engineering for power*, vol. 106, July 1984, pp. 542-551

[27] Jayesh M. Mehta and Suresh Goradia, "Experimental studies of the separated flow over a NASA GA(W)-1 airfoil," *AIAA Journal*, vol. 22, No. 4, April 1984, pp. 552-554

[28] S. J. Shamroth, H. Macdonald and W. R. Briley, "Predictions of cascade flow fields using the averaged Navier-Stokes equations," *Journal of Engineering for Gas Turbines and Power*, vol. 106, April 1984, pp. 383-390

[29] Day, I. J. and Cumpsty, N. A., "The Measurement and interpretation of flow within rotating stall cells in axial compressors," *Journal of Mechanical Engineering Sciences*, Vol. 20, No. 2, 1978, pp. 101-114

[30] Rhie C. M. and Chow W. L., "Numerical study of the turbulent flow past an airfoil with trailing edge separation," *AIAA Journal*, vol.21, No.11, November 1983, pp.1525-32

[31] Schlitching, "Boundary Layer Theory,".*McGraw Hill Book Company, England* 7th ed. 1987

[32] Wolfgang Rodi, "Turbulence Models and their Applications in Hydraulics," *State of the Art Paper. International Association of Hydraulic Research, University of Karlsruhe. Karlsruhe. FRG, 2nd edition* 1984

[33] C. Hircsh, "Numerical Computation of Internal and External Flows, ," *Wiley Series in Numerical Methods in Engineering. John Wiley and Sons Ltd., (Reprint) England.* Vol 2, 1991

[34] B. E. Launder and D. B. Spalding, "Lectures in Mathematical Models of Turbulence," *Academic Press Inc. (London)* 1972

[35] W. Rodi, "Examples of turbulence models for incompressible flows," *AIAA Journal*, vol. 20, No. 7, July 1982, pp. 872-879

[36] Suhas V. Patankar, "Numerical heat transfer and fluid flow," *Computational Methods in Mechanics and Thermal Sciences. Hemisphere Publishing Corporation. McGraw Hill Book Company* 1980

[37] C. T. Shaw, "Using Computational Fluid Dynamics," *Prentice Hall International (UK) Ltd.* 1992

[38] Joe D. Hoffman, "Numerical Methods for Engineers and Scientists," *McGraw Hill Book Company* 1992

[39] C. Hircsh, "Numerical Computation of Internal and External Flows," *Wiley Series in Numerical Methods in Engineering, John Wiley and Sons Ltd., (Reprint) England*, Vol. 1, 1991

[40] Joseph M. Verdon, "Unsteady Aerodynamics for Turbomachinery Aeroelastic Applications,". In David Nixon editor,*Unsteady Transonic Aerodynamics*, Progress in Aeronautics and Astronautics Vol 120, by AIAA Inc. 1989

[41] Harwood A. Hegna, "Numerical solution of incompressible turbulent flow over airfoils near stall," *AIAA Journal*, vol. 20, No. 1, January 1982, pp. 29-30

[42] G. Jin and M. Braza, "Two equation turbulence model for unsteady separated flow around airfoils," *AIAA Journal*, vol. 32, No. 11, November 1994, pp. 2316-2320

[43] Tuncer Cebeci (Editor), "Numerical and Physical aspects of Aerodynamic Flows II,*Spring-Verlag New York Inc.* 1984

Vitae

- Muhammad Naweed Ahmed
- Born in 1970 at Karachi, Pakistan.
- Received Bachelor of Engineering (**B.E.**) degree in Mechanical engineering from N.E.D. University of Engineering and Technology, Karachi, Pakistan in 1993.
- Received Master of Science (**M.S.**) degree in Mechanical Engineering from KFUPM, Saudi Arabia in 1995.